Summer 2022

Structural Characterization of Factor VIII-Inhibitor Complexes and Factor VIII Lipid Binding Mechanics

Corbin Mitchell
Western Washington University, corbinm72@gmail.com

Structural Characterization of Factor VIII-Inhibitor Complexes and Factor VIII Lipid Binding Mechanics

By

Corbin Mitchell

Accepted in Partial Completion
of the Requirements for the Degree
Master of Science

ADVISORY COMMITTEE

Chair, Dr. P. Clint Spiegel

Dr. John Antos

Dr. Jeanine Amacher

GRADUATE SCHOOL

David L. Patrick, Dean

Master's Thesis

In presenting this thesis in partial fulfillment of the requirements for a master's degree at Western Washington University, I grant to Western Washington University the non-exclusive royalty-free right to archive, reproduce, distribute, and display the thesis in any and all forms, including electronic format, via any digital library mechanisms maintained by WWU.

I represent and warrant this is my original work and does not infringe or violate any rights of others. I warrant that I have obtained written permissions from the owner of any third party copyrighted material included in these files.

I acknowledge that I retain ownership rights to the copyright of this work, including but not limited to the right to use all or part of this work in future works, such as articles or books.

Library users are granted permission for individual, research and non-commercial reproduction of this work for educational purposes only. Any further digital posting of this document requires specific permission from the author.

Any copying or publication of this thesis for commercial purposes, or for financial gain, is not allowed without my written permission.

Corbin Mitchell

07/22/2022

Structural Characterization of Factor VIII-Inhibitor Complexes and Factor VIII Lipid Binding Mechanics

A Thesis
Presented to
The Faculty of
Western Washington University

In Partial Fulfillment
Of the Requirements for the Degree
Master of Science

by
Corbin Mitchell
July 2022

Abstract

Blood coagulation factor VIII (FVIII) is a crucial protein cofactor within the blood coagulation cascade and facilitates the proteolytic activation of factor X by activated factor IX. During coagulation FVIII is activated and binds, via its C1 and C2 domains, to activated platelet membranes coordinated by interactions with exposed phosphatidylserine on the membrane surface. A deficiency of functional FVIII within a patient's bloodstream leads to the blood disorder hemophilia A, which results in prolonged bleeding episodes. Current treatment for hemophilia A relies on FVIII replacement therapy via the injection of exogenous FVIII. The main complication which arises from FVIII replacement therapy is the development of pathogenic anti-FVIII inhibitory antibodies, which bind to various regions of FVIII disrupting FVIII's ability to properly interact with its key binding partners, thereby nullifying treatment.

This thesis reports determination of low resolution SAXS envelopes and progress towards obtaining atomic resolution molecular structures of full length FVIII in complex with five different anti-A2 inhibitors, and a human derived anti-C1 inhibitor, NB2E9, in complex with the lone C1 domain. Solving the structure of one of these complexes would provide insight into the mechanism of inhibition for the A2 domain that would be invaluable when designing bioengineered hemophilia A therapeutics. This thesis further reports mutational studies of FVIII's C1C2 domains, yielding progress towards identifying docking and undocking conformations, represented by ~35-45^{o} rotation of the C2 hydrophobic loops. This utilized designing mutant constructs to form a disulfide bond which locks C1C2 in the proposed undocking conformation to compare lipid binding affinities, to build our understanding of the mechanism of lipid association and dissociation.

Acknowledgements

The work outlined in this document was conducted from Fall 2020 to Summer 2022 in Dr. P. Clint Spiegel's lab group at Western Washington University. Of the numerous students that have worked in the Spiegel lab I believe that my experiences have been made truly unique by the COVID-19 pandemic. I would like to express my appreciation and thanks to Clint for giving me the opportunity to join his research lab despite my applying to the program months after the deadline in the midst of a global pandemic, and never having exchanged a word of correspondence. The experiences I have been able to gain from my time at WWU have altered and shaped my life's trajectory only for the better, and for that I will be forever grateful to Clint. Secondly, I must express my sincerest thanks to Shaun Peters whom I consider a great friend and mentor, who trained and helped me begin my path as a researcher. Beyond this, Dr. Kenny Childers must be acknowledged, the post doc in our lab who we will joke about being our interim PI. Without Kenny's support and guidance the entirety of our lab would be adrift in a sea of confusion. The work and joyous nature of Kenny makes the intimidating unknown of research all the more comforting. I must also extend my appreciation to both Jordan Vaughn and Nathan Avery, who assisted in the work outlined in this document, and continued it following my departure. Both Jordan and Nathan are incredible individuals for whom I see nothing but success in their futures. Beyond these individuals the entirety of the Spiegel lab deserves credit, it is incredible to me the welcoming and merry culture that each and every member contributes to and the learning environment that this brings.

I must also extend my sincerest gratitude to both of my parents, Erin and Deven Mitchell, for their continued support as I continue my educational career. The pair of them both have taught me a love for expanding my knowledge and skills in a multitude of branches while providing me with all the tools I need to succeed. Thanks to Clint and the whole of the Spiegel lab.

Table of Contents

List of Figures and Tables

Abbreviations

ALS	Advanced Light Source
AOF	Animal Origin Free
ATP	Adenosine Triphosphate
BCSB	Berkeley Center for Structural Biology
BLI	Biolayer Interferometry
BU	Bethesda Unit
CDR	Complementarity Determining Regions
CV	Column Volume
DOE	Department of Energy
DOPC	1,2-dioleoyl-sn-glycero-3-phosphocholine
DOPS	1,2-dioleoyl-sn-glycero-3-phospho-L-serine
DTT	Dithiothreitol
EDTA	Ethylenediaminetetraacetic Acid
ELISA	Enzyme-Linked Immunosorbent Assay
ESI	Electrospray Ionization
F8	Factor VIII's Gene
Fab	Fragment Antigen-Binding
FC	Crystallizable Fragment, Tail of the Antibody
F(Roman Numeral)	Factor (Roman Numeral) i.e., FVIII is Factor VIII
F(Roman Numeral)a	Activated Factor (Roman Numeral) i.e., FVIIIa is Activated Factor VIII
FPLC	Fast Protein Liquid Chromatography
FT	Flowthrough
HBS	Histidine Buffer Solution
HEPES	4- (2-hydroxyethyl)-1-piperazineethanesulfonic acid)
hFVIII	Human Factor VIII

HPLC	High Performance Liquid Chromatography
HSP70	Heat Shock Protein 70
HWI	Hauptman-Woodward Medical Research Institute National High-Throughput Crystallization Center
IAA	Iodoacetamide
IDAT	Integrated Diffraction Analysis Technologies
IEC	Ion Exchange Chromatography
IgG	Immunoglobulin G
IgSF	Immunoglobulin Super Family
IMAC	Immobilized Metal Affinity Chromatography
IPTG	Isopropyl B-D-thiogalactopyranoside
ITI	Immune Tolerance Induction
LC	Liquid Chromatography
mAb	Monoclonal Antibody
MedE	Medium E
MS	Mass Spectrometry
MSP1D1	Membrane Scaffold Protein 1D1
NIH	National Institutes of Health
NTA	Nitriloacetic Acid
OD	Optical Density
OPDS	D-Isomer of Phosphatidylserine
OPLS	L-Isomer of Phosphatidylserine
PBS	Phosphate-Buffered Saline
PEG	Polyethylene Glycol
pFVIII	Porcine FVIII
PI	Isoelectric Point
PMSF	Phenylmethylsulfonyl Fluoride

PS	Phosphatidylserine
Q-TOF	Quadrupole-Time of Flight
SAXS	Small Angle X-Ray Scattering
SDS-PAGE	Sodium Dodecyl Sulfate-Polyacrylamide Gel Electrophoresis
SEC	Size Exclusion Chromatography
TEV	Tobacco Etch Virus
TRX	Thioredoxin
UV	Ultraviolet
v/v	Volume/Volume
vWF	Von Willebrand Factor
WT	Wilde Type
Xase	Tenase

Introduction

Hemostasis is the mechanism by which an organism can halt blood loss at the site of vascular injury while simultaneously maintaining normal blood flow elsewhere in the body. There are two pieces to the hemostasis mechanism, primary and secondary hemostasis. Primary hemostasis begins immediately following vascular injury, where bleeding is stopped via the formation of a hemostatic plug. This plug is constructed of aggregated platelets which aggregate and bind to the site of injury. Secondary hemostasis refers to the formation of an insoluble cross-linked fibrin mesh which is incorporated into and around the platelet plug strengthening and stabilizing the blood clot[1]. This work focuses on the secondary hemostasis mechanism, which is driven via protein blood coagulation factors[2]. These coagulation factors play crucial roles within the blood coagulation cascade, with a loss of these proteins' function leading to blood disorders, more commonly known as hemophilia. Patients who have hemophilia are unable to properly form blood clots, which leads to potentially life-threatening bleeding episodes. Specifically, hemophilia A is the result of a deficiency of functional factor VIII (FVIII), a key coenzyme involved in the intrinsic coagulation cascade. FVIII's activity is dependent on its ability to properly interact with several key binding partners and if these interactions are hindered the result is a loss of function. The work outlined in this thesis focuses on FVIII.

Primary Hemostasis

During primary hemostasis, a soft plug is formed via platelet aggregation and adhesion to the site of injury[1]. This plug then serves as the scaffolding for the congregation of blood

coagulation factors during secondary hemostasis, where they act to form a more stable hard fibrin clot[2].

Platelet Adhesion

The first step of primary hemostasis begins with the exposure of platelets to the subendothelial matrix following vascular injury, which triggers the adhesion and activation of platelets to form a soft clot[2]. There are multiple receptors on the surface of platelets that play a role in adhesion, with multiple adhesive proteins interacting with each receptor. Each of these receptors have regulation mechanisms such that platelet adhesion only occurs following vascular injury[6, 7, 8]. Von Willebrand factor (vWF) is a multimeric glycoprotein made up of three A domains, three B domains, two C domains, and four D domains and mediates platelet adhesion to exposed vascular sub-endothelium and the subsequent platelet aggregation. Upon vascular injury, vWF binds to the damaged vessel walls, specifically binding to fibrillar collagen type I and III via the A3 domain and collagen type VI via the A1 domain[9]. Once immobilized, vWF's A1 domain binds to platelets via the glycoprotein Ib-IX-V (GPIb-IX-V) receptor complex. Once bound, the platelets adhere to the exposed collagen of the vessel wall via the glycoprotein VI receptor (GPVI)[8].

Platelet Aggregation

Once bound to the vessel walls via vWF, the platelets begin to aggregate through platelet-platelet interactions. This occurs following a conformational shift in the integrin αIIbβ3 receptor, which allows for the receptor to bind to fibrinogen resulting in platelet aggregation[11]. Additionally, during this process platelets are activated, during which scramblase acts to flip

negatively charged phosphatidylserine between the platelet lipid bilayers. This results in an increase in the negative charge in the outer leaflet of platelet membranes[12]. These activated platelet membranes then serve as a surface for secondary hemostasis to form a fibrin clot via the blood coagulation factors.

Secondary Hemostasis

Secondary hemostasis refers to the formation of a hard fibrin clot and is traditionally depicted by the blood coagulation cascade model. The coagulation cascade maps out the series of protein interactions which lead to the proteolytic activation of clotting factors and ultimately the cleavage of fibrinogen to fibrin to form a hard fibrin clot. This catalytic cascade is divided into the extrinsic and intrinsic pathways which join at a common pathway[11] (Figure 1).

However, this model is insufficient in describing the dynamic nature of these subsections as they act within the overarching coagulation cascade. To account for this, a cell-based model which breaks the coagulation cascade into three distinct but overlapping phases: initiation, amplification, and propagation, has been developed to account for the dynamic nature of this mechanism[11].

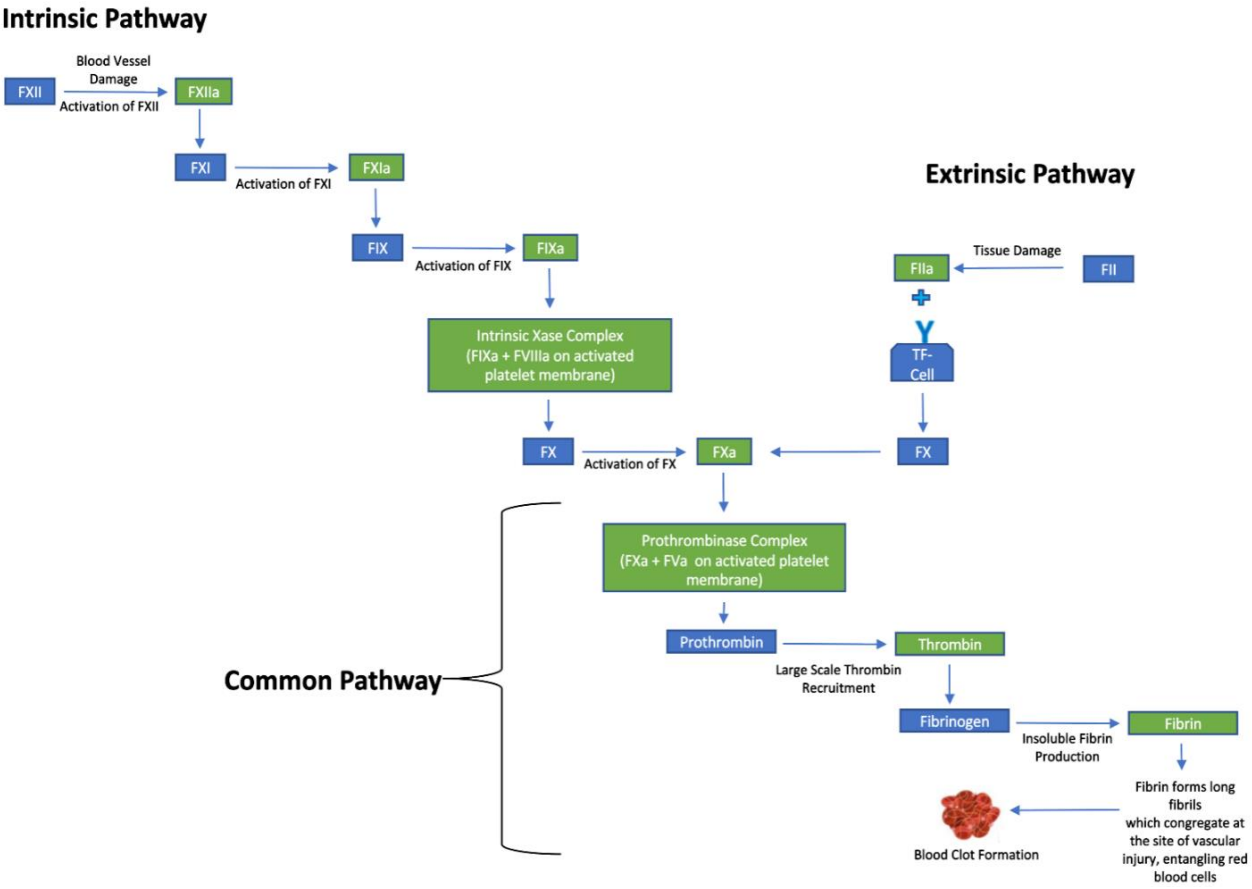

Figure 1. Blood coagulation cascade. The traditional model for blood coagulation, comprised of both an intrinsic and extrinsic pathway which converge at a final common pathway, resulting in the generation of fibrin, leading to the formation of a hard clot. FXIIa then begins an enzymatic activation cascade, generating FXIa, which generates FIXa. FIXa then forms the intrinsic tenase complex with its cofactor, FVIIIa (generated during amplification). The extrinsic pathway is initiated by tissue damage, activating FVII. FVIIa then forms a complex with TF, this TF-FIIA complex and the tenase complex act to proteolytically cleave and thereby activate FX on the surface of activated platelets during the final common pathway. The generated FXa then forms the prothrombinase complex with its cofactor, FVa (generated during amplification), which acts to generate high amounts of thrombin. The generated thrombin then proteolytically converts the soluble fibrinogen to the insoluble fibrin which assembles into long fibrils that gather at the site of vascular injury to provide mechanical support to form a stable, hard blood clot.

Initiation

Primary hemostasis begins with the initiation phase (extrinsic coagulation pathway) following tissue damage which results in the expression of tissue factor (TF), an integral membrane protein of endothelial cells. Following TF expression, activated factor VII (FVIIa)

quickly binds to the exposed TF[14]. Keep in mind that FVII is the only coagulation protein that is regularly found in circulation in its activated form, with approximately 1% of the FVII in the bloodstream being FVIIa[15].This TF-FVIIa complex then acts to activate additional FVII leading to a positive feedback loop in the formation of the TF-FVIIa complex[11]. Notably TF is the only coagulation protein, which is permanently attached to the membrane surface, and so acts to anchor this complex to the surface of TF-bearing cells[17]. Thus, the initiation step is localized to TF-bearing cell surfaces at the site of injury.

Beyond activating additional FVII, the TF-FVIIa complex acts to activate small amounts of factor IX (FIX) and factor X (FX). Factor V (FV) is then directly activated by FXa; however, this process occurs slowly and little FVa is recruited. The generated FXa then binds to the few molecules of its cofactor, FVa, that were generated, forming the prothrombinase complex on the surface of TF-bearing cells. This prothrombinase complex then proteolytically cleaves prothrombin generating a small amount of thrombin[11] (Figure 2).

Phase 1: Initiation

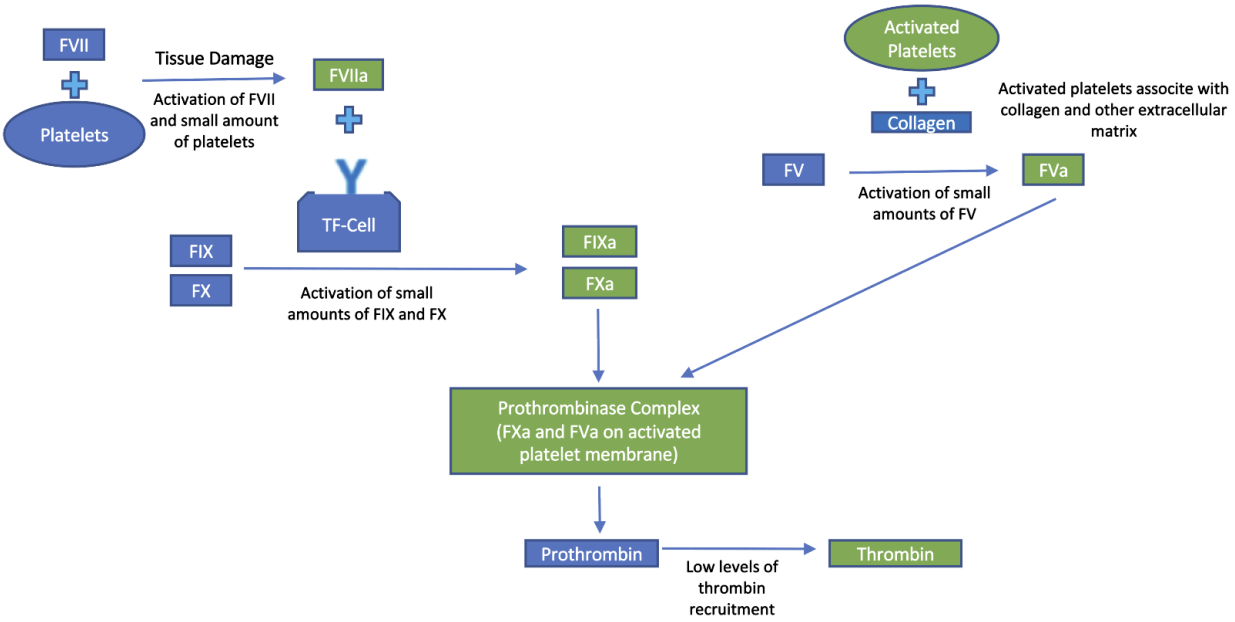

Figure 2. Phase 1 of secondary hemostasis, initiation. Secondary hemostasis is divided into three distinct, yet overlapping phases: initiation, amplification, and propagation. Initiation begins following tissue damage, which results in the activation of FVII and platelets. Tissue factor, located on the surface membrane of endothelial cells binds to FVIIa, the resulting FVIIa-TF complex activates small amounts of FIX, FX and FVII. Activated platelets bind to collagen and activate FV, leading to the formation of the prothrombinase complex (FXa and FVa) on the surface of TF-bearing cells. Prothrombinase then produces small amounts of thrombin, which is used during the amplification phase.

Amplification

During the second phase of secondary hemostasis, amplification, the thrombin generated during the initiation phase diffuses away from the TF-bearing cells and acts to activate factors V, VIII and XI. Additionally, the thrombin binds to and further activates platelets, causing an increase in the negative phosphatidylserine headgroups on platelet membrane surfaces[19] (Figure 3). This activation of the blood coagulation factors, and platelet membranes generates all the necessary components to begin the large-scale thrombin production seen in the final phase, propagation.

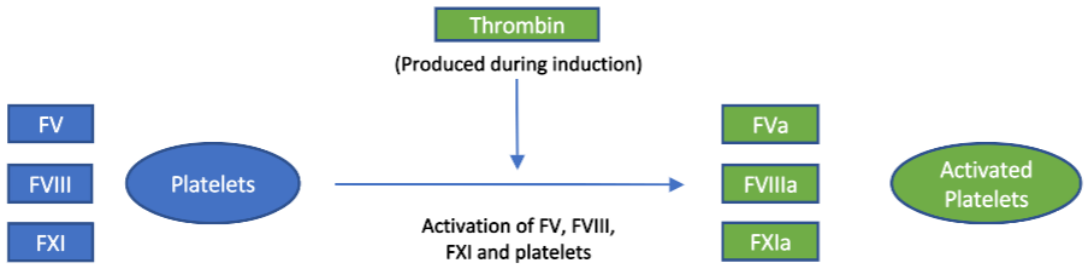

Figure 3. Phase 2 of secondary hemostasis, amplification. During amplification, the thrombin generated during the initiation phase diffuses away from the TF-bearing cells where it originated and acts to generate FVa, FVIIIa, FXIa, and activated platelets. These activated coagulation factors and platelets are then utilized for large-scale thrombin recruitment during the final stage, propagation.

Propagation

The third phase, propagation, occurs on the surface of the newly activated platelet membranes. This phase is also known as the intrinsic pathway within the blood coagulation cascade. During the propagation phase large bursts of thrombin are produced, which then convert the soluble plasma protein fibrinogen into insoluble fibrin. This fibrin is then crosslinked together and congregates at the site of injury to form an insoluble fibrin mesh that adds mechanical strength to the soft clot formed during primary hemostasis[20].

The protein coagulation interactions which drive this process begins with the contact of factor XII (FXII) to the negatively charged activated platelet membrane resulting in FXII being activated (FXIIa), which then activates FXI. FXI is also activated by thrombin in the presence of a negatively charged surface, as well as being activated by FXIa in a positive feedback loop[21]. FXIa then activates FIX[22]. Thrombin also activates FVIII which acts as a cofactor for the serine

protease FIXa, both of which associate to negatively charged platelet membranes and bind to one another, forming the intrinsic Xase (tenase) complex. This complex proteolytically cleaves and activates FX[23]. Following this, FXa associates to FVa on the activated platelet membrane to form the prothrombinase complex, which cleaves prothrombin, converting it to thrombin at large-scale[24]. The generated thrombin further cleaves the soluble fibrinogen to insoluble fibrin as well as activates FXIII. FXIIIa then acts to form long crosslinked fibrils of this insoluble fibrin which congregate at the site of injury, forming the insoluble fibrin mesh, resulting in a stabilized blood clot[82] (Figure 4).

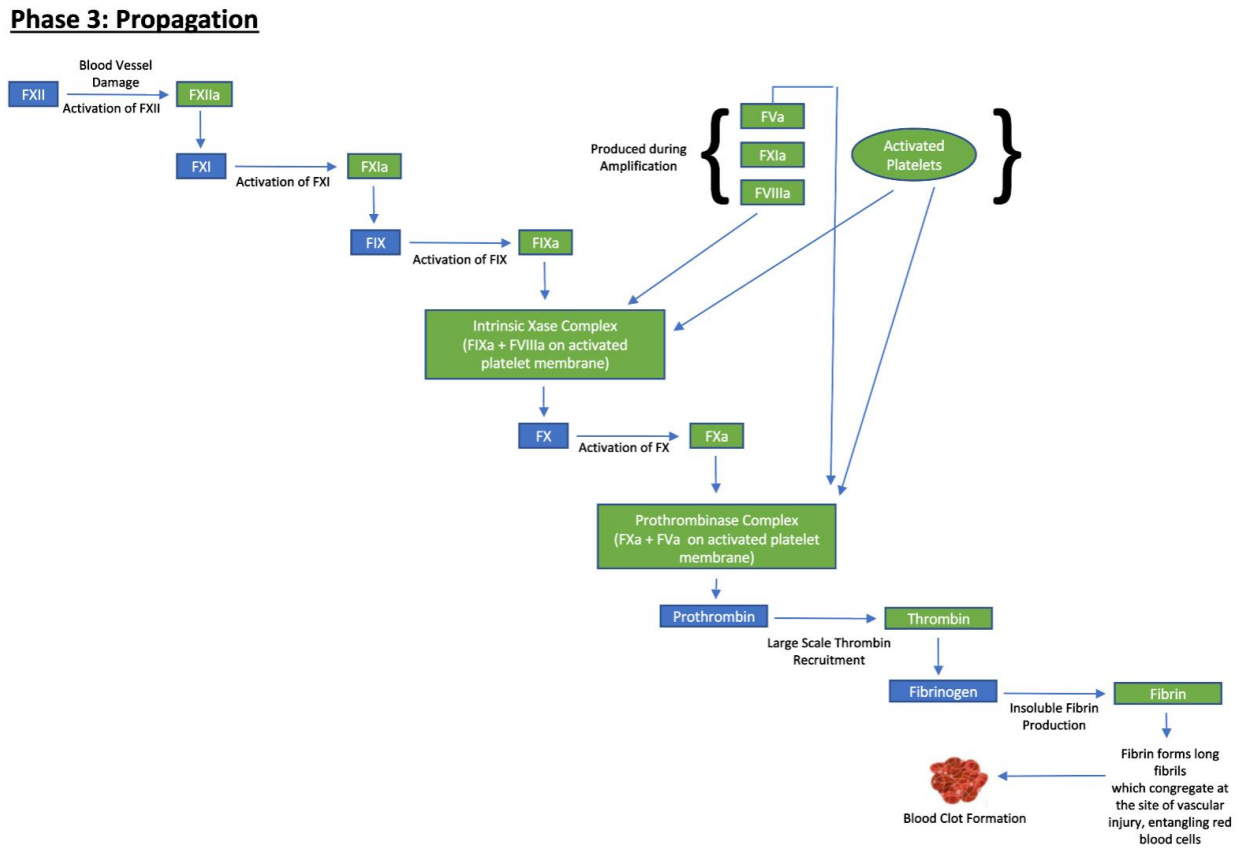

Figure 4. Phase 3 of secondary hemostasis, propagation. Propagation, otherwise known within the traditional blood coagulation cascade as the intrinsic pathway, is stimulated by vascular damage, resulting in the activation of FXII. FXIIa then begins an enzymatic activation cascade, generating FXIa, which generates FIXa. FIXa then forms the intrinsic tenase complex with its

cofactor, FVIIIa (generated during amplification), and acts to proteolytically cleave and thereby activate FX on the surface of activated platelets. FXa then forms the prothrombinase complex with its cofactor, FVa (generated during amplification), which acts to generate high amounts of thrombin. The generated thrombin then proteolytically converts the soluble fibrinogen to the insoluble fibrin which assembles into long fibrils that gather at the site of vascular injury to provide mechanical support to form a stable, hard blood clot.

Table 1. Blood Coagulation Factors and Associated Proteins

Blood Coagulation Factors and Associated Proteins	**Function**
Factor I (fibrinogen)	Precursor to fibrin
Factor II (prothrombin)	Once activated (FIIa/Thrombin) activates FI, FV, FX, FVII, FVIII, FXI, FXIII, protein C, platelets
Factor III (tissue factor)	Cofactor for FVIIa
Factor IV (calcium)	Required for coagulation factors to bind to phospholipids
Factor V	Cofactor for FX, which when bound forms the prothrombinase complex
Factor VII	Activates FIX, FX
Factor VIII	Cofactor of FIX, which when bound forms the intrinsic tenase complex
Factor IX	Activates FX, forms intrinsic tenase complex with FVIII
Factor X	Activates FII, forms prothrombinase complex with FV
Factor XI	Activates FIX
Factor XII	Activates FXI, FVII
Factor XIII	Crosslinks fibrin
von Willebrand factor	Binds to and guards against premature clearance/proteolytic degradation of FVIII, mediates platelet adhesion
Protein C	Inactivates FVa and FVIIIa
Protein S	Cofactor for activated protein C

Blood Coagulation Factor VIII

FVIII is a glycoprotein expressed in and secreted from both liver sinusoidal cells and endothelial cells acting as an essential cofactor for FIXa within the blood coagulation cascade. A lack of functional FVIII results in a reduction of FIXa's activity by 200,000-fold, causing the blood coagulation cascade to come to a halt[25]. The factor FVIII gene, F8, is located on the X chromosome and is comprised of 186,000 base pairs. The encoded full length FVIII protein is 2332 amino acids long with a domain organization of A1-a1-A2-a2-B-a3-A3-C1-C2, with the A domains having short spacers (a1, a2, a3) which contain acidic regions with clusters of Asp and Glu residues. Upon secretion from endothelial cells, but prior to circulation, a portion of the B domain is cleaved and removed between Arg1313 and Arg1648, resulting in a heterodimer between the light (a3-A3-C1-C2) and heavy chains (A1-a1-A2-a2-B) of FVIII[26] (Figure 5).

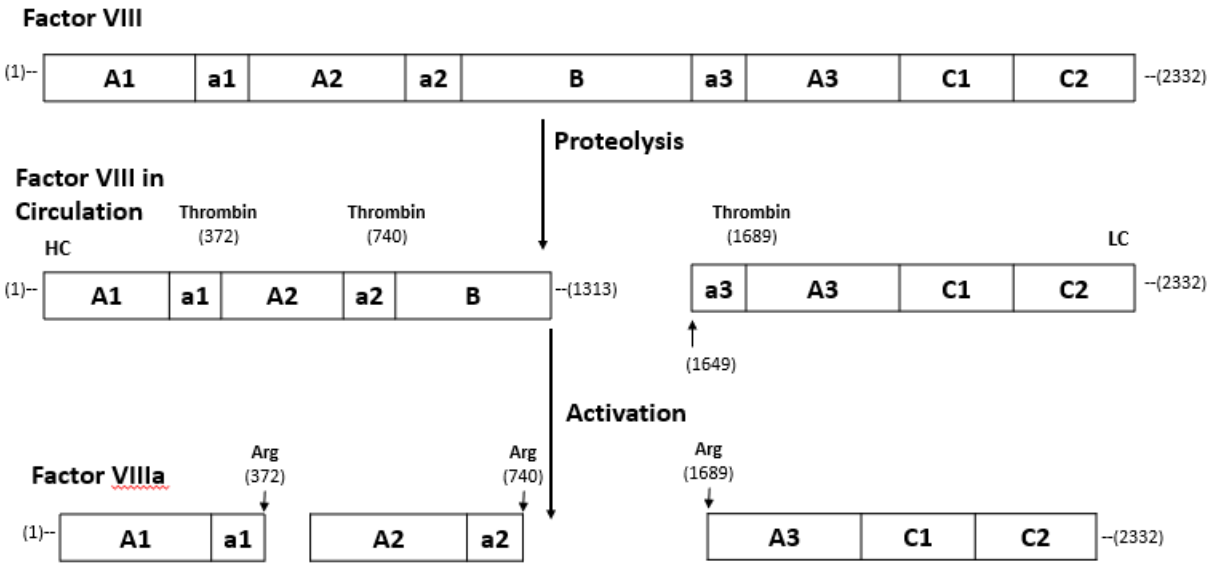

Figure 5. A schematic view of FVIII as it moves from its initial construct to its activated form. First, FVIII is synthesized in endothelial cells forming a single 2332 residue polypeptide chain with the following domain organization: A1-a1-A2-a2-B-a3-A3-C1-C2. The a1, a2 and a3

domains are acidic linker regions. Prior to circulation FVIII is cleaved at Arg1313 and Arg1648 resulting in the formation of a heterodimer between the light (a3-A3-C1-C2) and heavy chains (A1-a1-A2-a2-B). FVIII is then activated by thrombin which cleaves at Arg372, Arg740 and Arg1689, resulting in FVIII activation. Modified from Mazurkiewicz-Pisarek et al., 2016

During circulation, the light chain of FVIII is tightly bound via noncovalent interactions to vWF. vWF acts to maintain FVIII's stability while in circulation by preventing proteolytic degradation and premature clearance from the blood stream, while also serving to block non-specific phospholipid binding. Upon vascular injury, FVIII is proteolytically cleaved by thrombin, and the remainder of the B domain and a3 spacer are removed, activating FVIII (Figure 5). This activation leads to the dissociation of FVIIIa from vWF[24]. Following activation and dissociation from vWF, FVIIIa associates to activated platelet membranes where it acts as a cofactor for FIXa in the proteolytic cleavage and subsequent activation of FX[24, 29]. Following activation by thrombin FVIIIa is inactivated by activated protein C (APC) and its cofactor protein S. This inactivation comes about as a result from APC's cleavage of FVIIIa's A1 and A2 domains at Arg336 and Arg562[27].

FVIII C Domains

A structure of the B-domain deleted FVIII was first solved in 2008 with a resolution of 3.7 Å. This structure implied a difference in the flexibility of the two C domains. The C2 domain was found to be more loosely bound to the rest of the overall protein, forming 400 $Å^2$ and 200 $Å^2$ of interfaces between the C1 and A3 domains, respectively, for a total 600 $Å^2$ of total contact. The C1 domain is more tightly bound, with a 1200 $Å^2$ of hydrophobic interface with the A3 domain, for a total of 1400 $Å^2$ [62]. The flexibility of the C2 domain was confirmed in 2020,

with the publication of the high-resolution structure of a FVIII therapeutic, ET3i. This structure was crystalized with two proteins in the asymmetric unit, which allowed for two structures to be compared. Notably, these two ET3i molecules were in differing conformations dubbed model A and model B. Model A was in a conformation previously see in literature while a new conformation was found in model B. The conformation identified in model B was found to have residues rotated ~35-45 degrees around a central set of core residues, with shifts of individual residues up to 14 Å[45](Figure 6). The flexibility of the C2 domain implies the possibility of two distinct motifs of FVIII. One in which FVIII binds to activated platelet membranes, and the other which acts as a non-binding conformation. The C domains of FVIII are structurally homologous to one another, containing common structural features such as two hydrophobic loops which extend beyond the overall globular fold at the bottom of the overall protein, and thought to be involved in lipid binding[63]. Notably, the affinity of recombinant C2 to phospholipids has been shown to have an approximate 40-fold decrease when compared to FVIII, suggesting the need for both C domains for optimal lipid binding[64]. Mutations of FVIII in any of its domains that disrupt its ability to function within the blood coagulation cascade can lead to a loss of functionality of the protein and by extension loss of coagulation ability of the entire cascade.

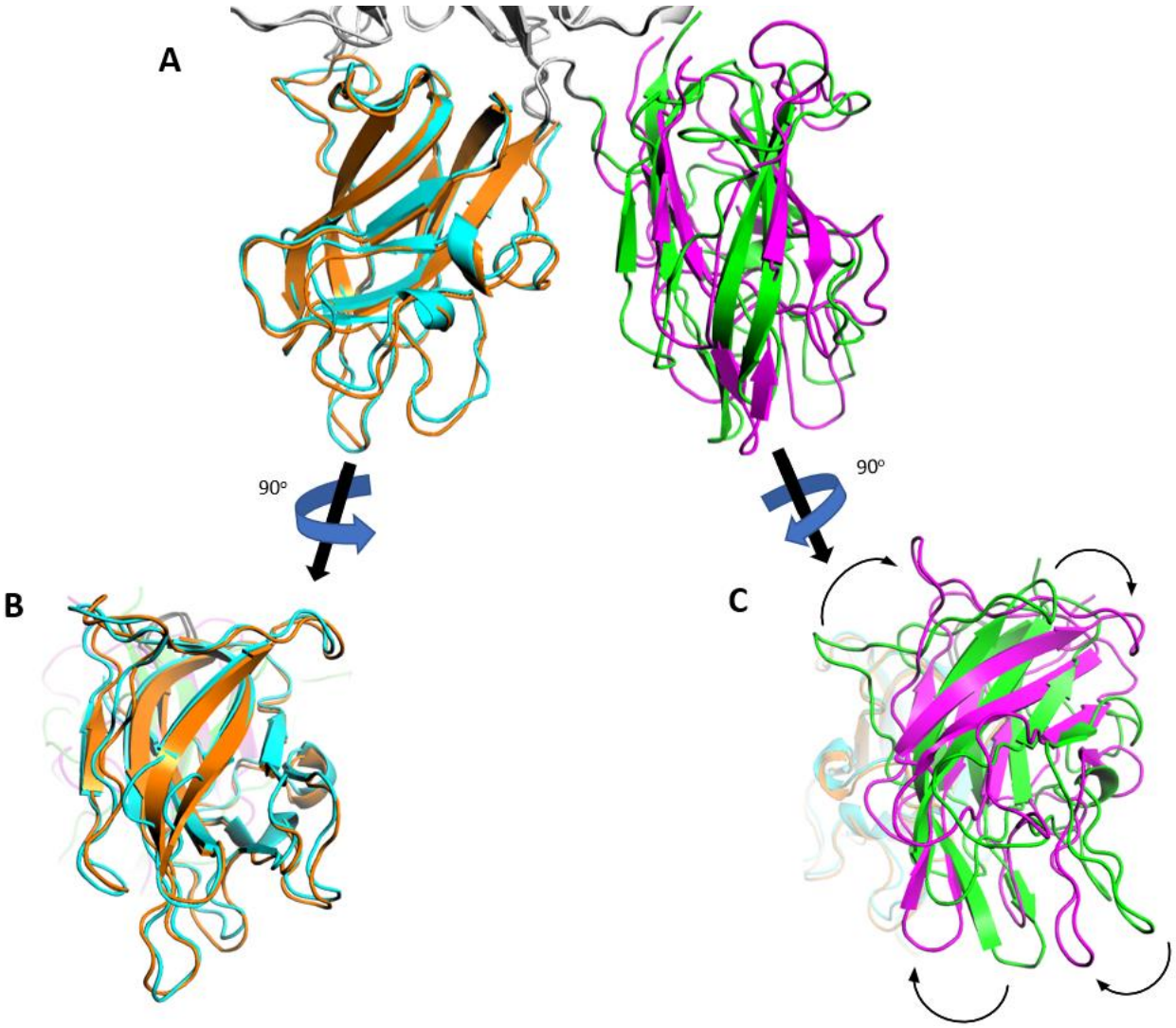

Figure 6. FVIII C2 domain flexibility. A) Structural alignment of FVIII C1 and C2 domains in proposed docking (model B) and undocking (model A); C1 model A: orange, C1 model B: cyan, C2 model A: green, C2 model B: purple. B) 90^{o} rotation to the left for side view of the C1 domain alignment. C: 90^{o} rotation to the right for side view of the C2 domain alignment, the C2 domain rotates around a set of central residues, resulting in a shift of the hydrophobic loops away from the C1 domain. Generated from PDB: 6MF0.

Hemophilia A

A deficiency in functional FVIII in a patient's bloodstream causes a bleeding disorder known as hemophilia A. Hemophilia A is a hereditary X-linked disorder which results in

improper blood clot formation, causing heavy bleeding episodes that can result in death. Approximately 1 in 5,000 males are born with hemophilia A each year. There are many different mutations of the F8 gene which can lead to varying loss of FVIII function, and thereby hemophilia A of varying levels of severity. These loss-of-function mutations range from complete loss of FVIII production, to single point mutations which disrupt FVIII's ability to properly interact with key binding partners (such as vWF, FIXa, activated platelet membranes). The severity of hemophilia A is defined by the residual level of functional FVIII found in a patient's blood; mild: 6-49%, moderate: 1-5%, severe: <1%[26.] Strikingly, about 60-70% of patients with hemophilia A are severe cases[32].

Beyond genetic complications, it is possible, although rare, for patients with functional FVIII to develop anti-FVIII inhibitory antibodies through an autoimmune response. These antibodies act to neutralize a patient's endogenous FVIII, causing a decrease in the residual levels of functional FVIII found in the blood. This results in what is known as acquired hemophilia A[33].

Hemophilia A Treatment

Currently, the main treatment for hemophilia A relies on regular direct infusions of plasma derived or recombinant FVIII, in a process known as FVIII replacement therapy. The dosage and frequency of infusion is dependent on the severity of the disorder and can cost in the in the range of $300,000-$500,000 per year, per patient[34, 35]. There are alternative drugs for treating hemophilia A currently available, however the most successful and most employed is

replacement therapy[36]. Yet, due to the need for frequent infusion, high cost, and treatment related complications there is ample opportunity for improvement in hemophilia A treatment.

Treatment Complications: Development of Inhibitory Antibodies

While effective in stopping bleeding episodes, frequent FVIII replacement therapy may give rise to the development of inhibitory antibodies by a patient's immune system, which act to neutralize the effect of the injected FVIII. The development of inhibitory antibodies is relatively common within highly treated patients with approximately 30% of those with severe hemophilia A developing inhibitory antibodies[26]. For those individuals who develop this complication from FVIII replacement therapy, or those with acquired hemophilia A, there are treatment options available.

Immune tolerance induction (ITI) is the only treatment method proven to work in the eradication of these inhibitors. ITI involves frequent injection of increasingly high doses of FVIII concentrate alongside prothrombin complex concentrates to control bleeding episodes, while trying to re-educate the immune system to tolerate the exogenous FVIII and cease production of inhibitors. If after 6 months there is not a sustained downward trend in inhibitor concentration within the blood, immunosuppressants are also prescribed[38, 26]. While ITI is successful in 60%-80% of patients it is quite costly and demanding, with an average duration of treatment of 18.7 months and an average total cost of $1,463,668 per patient[40]. Beyond this, ITI is not always successful, and even for those who see a reduction in antibody production there is always a risk of inhibitor recurrence[26].

Replacement therapy with porcine FVIII (pFVIII) is a second-line therapeutic for treating those with inhibitors due to the low cross-reactivity between pFVIII and anti-human FVIII

(hFVIII) antibodies[42]. In addition, pFVIII is a relevant FVIII replacement therapeutic in that it is more stable and active than hFVIII due to a tighter binding interaction between the A2 domain and activated pFVIII in comparison to hFVIII[43]. Novel human/porcine chimeric FVIII constructs have been made to identify which domains contribute to the improvements seen in pFVIII (Figure 7). The chimeric protein ET3i, which contains porcine A1 and A3 domains and human A2, C1 and C2 domains has been shown to have better expression and activity levels than hFVIII, both in vivo and in vitro expression systems. This was shown to be the result of a reduction in the interaction with unfolded protein response chaperones in the endoplasmic reticulum. Genetically engineered protein constructs such as ET3i are promising therapeutics to be able to mitigate the inactivation of FVIII during replacement therapy or in

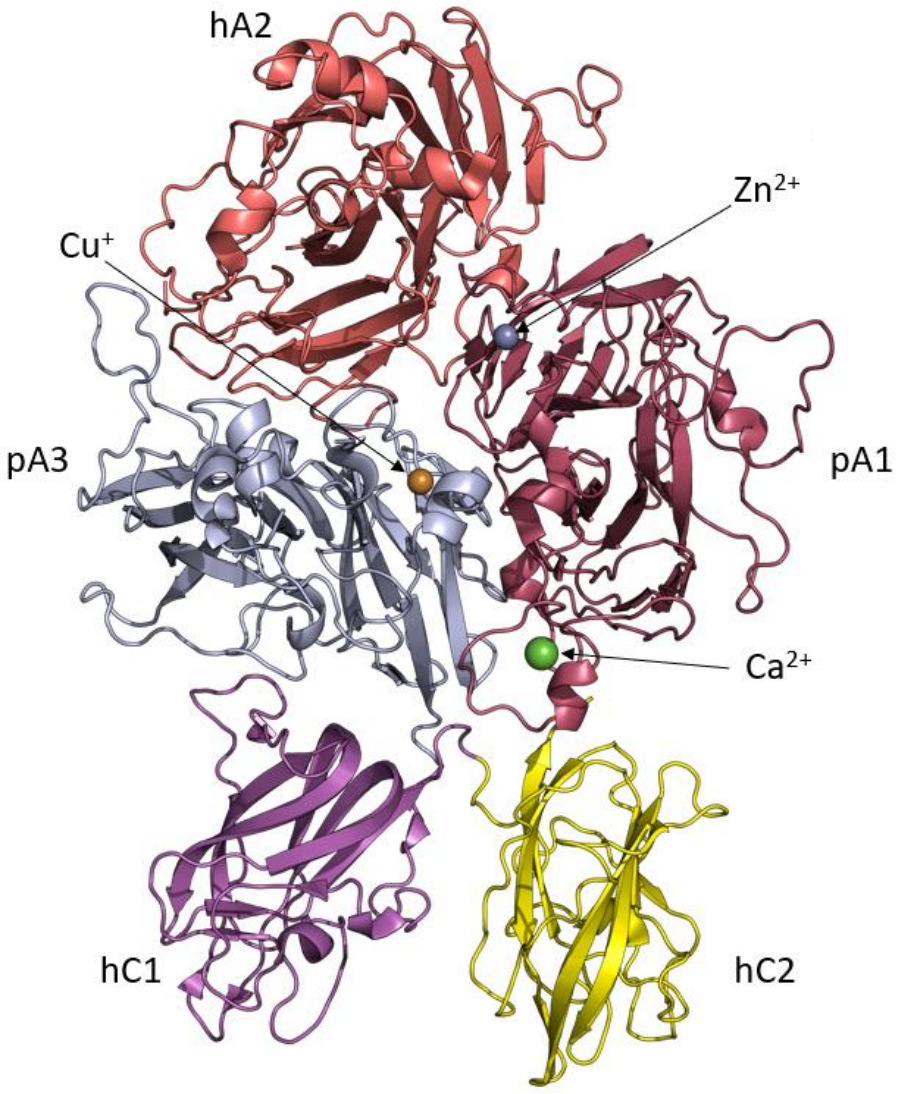

Figure 7. Ribbon diagram representation of ET3i structure. Showing the three human domains, hA2, hC1, hC2 in salmon, purple, and yellow, the two porcine domains (pA3 and pA2) shown in grey and raspberry. Three metal ions are embedded within the trimeric A domain assembly: Zn^{2+}, Cu^{+}, Ca^{2+} (PDBID#: 6MF0).

potential gene therapy applications[44].

FVIII Inhibitory Antibodies

Anti-FVIII antibodies are 150 kDa immunoglobulin G's (IgG), the most common variety of antibody found in circulation accounting for approximately 75% of all serum antibodies in humans[37]. These glycoproteins fall within the immunoglobulin super family (IgSF) and are comprised of a two heavy and two light chains. Each chain consists of a variable domain at its N terminus and a constant domain at its C terminus, bound together via disulfide bonds (Figure 8). Within each of the variable domains lies three hypervariable complementarity determining regions (CDR) which make up the antigen binding regions of the IgG, otherwise known as the paratope. These paratopes specifically bind to a substrate, the antigen, at a targeted region, the epitope[65]. IgGs are generated when a foreign protein within the bloodstream binds to B-cell surface antigen-receptors. The foreign protein is then taken up into the B-cell where it is degraded, and the generated fragments exposed to major histocompatibility II molecules. Helper T cells then cause the B-cell to produce specific antibodies against the exposed peptide fragments if these fragments are recognized as foreign[46]. The B-cell then produces clones, which produce more antibodies with minor mutations, where the clones that produce the highest affinity antibodies out-compete the others for survival. The B-cells that remain following this process are known as memory B cells, which when activated produce clones that secrete the given antibody. These cells are located within the spleen[47]. To produce FVIII inhibitory antibodies within the laboratory, mice are treated with human FVIII via venous injection to generate inhibitor producing B-cells. These B-cells are harvested from the mice and used to generate B-cell hybridomas by fusing myeloma cancer cells with the spleen cells of

inhibitor producing mice. These B-myeloma fusion cells serve to quickly divide allowing for rapid growth and antibody expression.

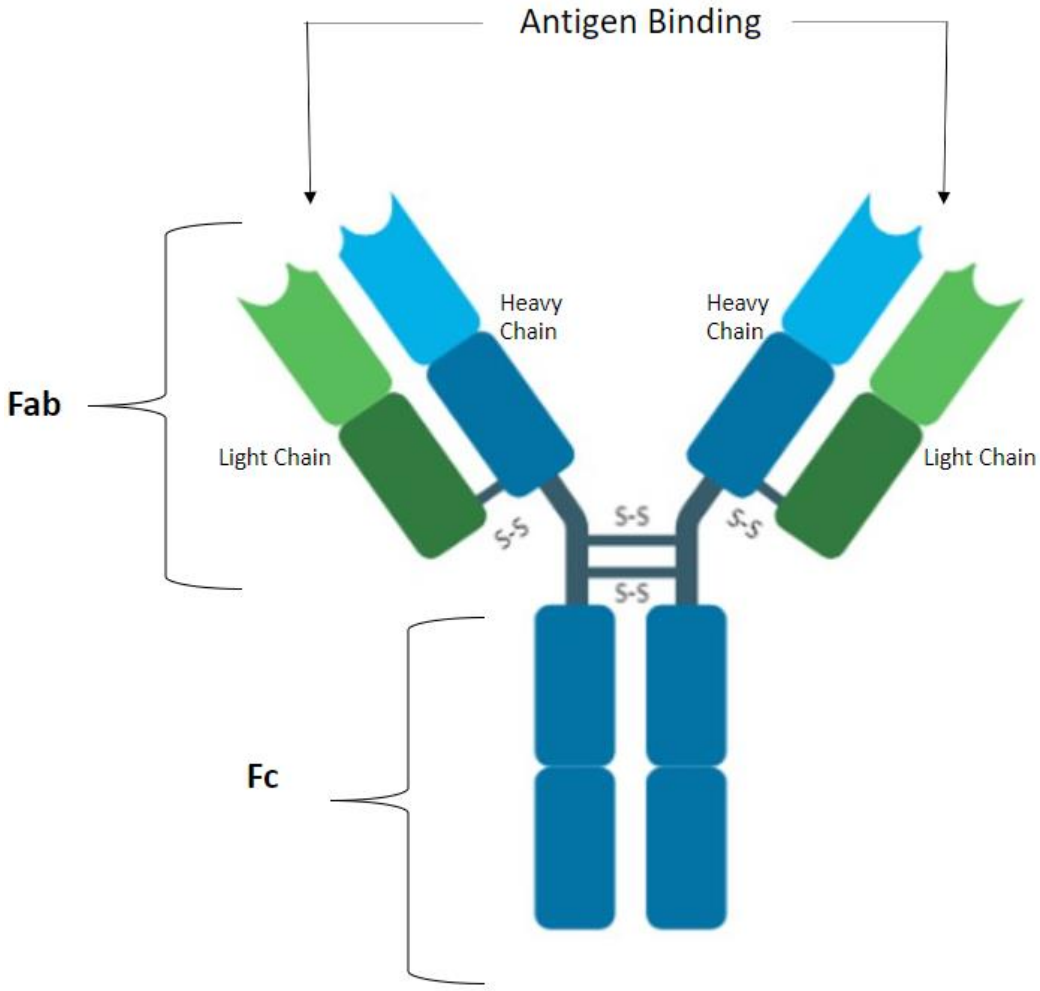

Figure 8. Basic structure of Immunoglobulin G. Depicts the heavy chain in blue and the light chain in green, with disulfide bridges labeled as S-S, and the Fab, Fc and antigen binding regions denoted in the figure.

Anti-FVIII antibodies are classified dependent on their kinetics and extent of inhibition of FVIII as either type I or type II inhibitors, and further classified based on their binding epitopes as various groups. Type I inhibitors follow second-order kinetics (linear relationship between inhibition and inhibitor concentration) and inactivate FVIII completely. Type II inhibitors have complex kinetics (non-linear inhibition) and incompletely inactivate FVIII. Inhibitory antibodies

primarily bind to the A2 and C2 domains of FVIII[40]. A2 inhibitors have been shown to inhibit FVIIIa by preventing the Xase complex from activating FX, but still allow binding to FX[49]. The binding epitope for these anti-A2 antibodies is thought to be within residues 373-606, however the details have yet to be defined structurally[50]. Anti-C2 antibodies are classified beyond types I and II, with the sub-classifications classical and non-classical. Non-classical anti-C2 antibodies do not disrupt phospholipid interactions, instead disrupting the activation of FVIII by interrupting interaction with FXa or thrombin, while classical inhibitors disrupt phospholipid binding[66]. Antibodies have been shown to also bind to the A3 and C1 domains with inhibitory action against FVIII, however the A2 and C2 are the most immunogenic[49].

Once bound to FVIII, inhibitors act to sterically block regions of FVIII resulting in loss of function[50]. Contained within these epitopes are binding sites for several key binding partners of FVIII including FIX, the phospholipid membrane of activated platelets, vWF, FXa and thrombin. Inhibitors can target multiple epitopes and the target epitopes can change over time[43]. A Bethesda assay is used to determine whether injected FVIII is functioning properly, or if a patient's immune system is neutralizing FVIII. Plasma from a patient undergoes a series of dilutions, FVIII is added, and coagulation times are measured, with the results being given in Bethesda units (BU). A BU is defined as the amount of inhibitor that eliminates half of FVIII activity per mL of normal plasma, within two hours, incubated at 37 ^{o}C[52]. For reference, a high responding inhibitor is defined as having more than five Bethesda units[53].

Antibodies of Study

Specifically, this study examines the anti-C1 human derived antibody NB2E9, and the following anti-A2 murine derived antibodies: 4A4, 4F4, 1-D4, 2-101, and 4C7. NB2E9 is a type II inhibitor in that it does not completely neutralize FVIII activity and has complex binding kinetics. NB2E9 binds to the C1 and A3 domains of FVIII and was derived from a patient where the antibody neutralized WT FVIII, but not the patients endogenous FVIII which contained a mutation at Arg2150, placing importance on this residue for NB2E9's binding epitope. NB2E9 acts to compete with vWF for binding to FVIII, which results in a time-dependent neutralization of FVIII activity[54]. The five anti-A2 antibodies are also defined as being inhibitory or non-inhibitory based on Bethesda assay and divided into either type I or type II dependent on the degree of inhibition and binding kinetics. 4A4, 4F4 and 1-D4 are all type I inhibitory antibodies, with 2-101 being a type II inhibitory antibody, and 4C7 being non-inhibitory. The A2 inhibitors can be further classified into the following epitope groups: A, AB, BCD, C, D, DE and E based on the pattern of overlap of their binding epitopes, as determined by ELISA. The various groups indicate overlap in regions on the A2 domain where antibody binding occurs, and thereby correspond to some level of commonality in their inhibition mechanisms. Most group A antibodies bind to a previously determined epitope bound by Arg484-Ile508 in the N-terminal region of A2, noncompetitively inhibiting binding to FIXa. Most group B and C antibodies show little to no inhibition. Group D and E bind epitopes in the C-terminal of A2. Group E inhibits the activation of FVIII by preventing thrombin from being able to cleave the FVIII light chain at Arg1689. 4A4 is group A, 4F4 is group B, and 1-D4 and 4C7 are group E (Table 2)[55].

Table 2. Anti-A2 Antibodies

Monoclonal Antibody	BU/mg IgG	Type	Group	Binding Epitope
4A4	40,000	I	A	Asp403-His444
4F4	330	I	B	Indeterminate
1-D4	7,000	I	E	Glu604-Arg740
2-101	11,000	II	?	His444-Arg541
4C7	<1	Non-inhibitory	E	Indeterminate

While there is a seemingly never-ending variety of possible anti-FVIII inhibitory antibodies which may develop in a patient, the most important aspect is the location of inhibitory binding epitopes, and thereby the mechanism of inhibition. Neutralizing antibodies prevent FVIII function by sterically blocking key interactions which are necessary for proper FVIII functionality. Therefore, it is of significant interest in the ongoing development of hemophilia A treatments to obtain structural data of FVIII's interactions with inhibitory antibodies. Doing so not only provides insight into the residues which play a role in the specific inhibitory antibodies' binding epitopes, but also a more comprehensive view of what residues of FVIII are necessary for proper function, and therefore must remain spatially unhindered to maintain this functionality. Notably, obtaining the first structures of FVIII in complex with anti-A2 inhibitors and the C1 domain in complex with a human derived antibody will provide insight into the inhibition mechanism of one of the two most immunogenic domains of FVIII as well as confirm methods of inhibition generated with mouse derived antibodies via the C1 domain. This information may provide valuable insight that would be crucial when designing bioengineered FVIII therapeutics and in understanding the role of the A2 domain in terms of FVIII function.

Structural Investigations of FVIII-Antibody Complexes

Previous work to analyze the structure of FVIII in complex with inhibitory antibodies has been done via x-ray crystallography as well as small angle x-ray scattering (SAXS)[48, 49]. X-ray crystallography is dependent upon being able to crystalize your protein or proteins of interest. Once crystals are obtained, they are exposed to x-rays, resulting in diffraction patterns that can be utilized to gain information about the packing symmetry and size of the repeating crystalline unit (protein) which can be used to gain knowledge of a protein's structure[56]. The limiting step within this process is the formation of a high enough quality protein crystal to obtain diffraction data. This is typically done via hanging drop vapor diffusion. Not only do you have to obtain high enough concentrations of sample and find the proper environmental conditions to cause protein crystallization, but you must also wait for a crystal to form which can take anywhere from 10 minutes to a year[51]. This has been successful when working with FVIII in complex with inhibitory antibodies in the past, but difficulty in complex production and crystallization varies for any given complex[58]. Alternatively, SAXS has also been employed to examine the structures of FVIII complexes. Unlike x-ray crystallography, SAXS does not require the crystallization of protein. Instead of examining the diffraction pattern of a protein crystal, SAXS relies on the elastic scattering behavior that x-rays display when traveling through a material and analyzing the resulting scattering angles. This is accomplished by shining x-rays through a liquid sample and recording these scattering angles[59]. Furthermore, SAXS, unlike crystallography, allows for the investigation of conformational shifts with a protein without needing to generate structures from different samples. However, this is a result of spatial averaging that is employed when analyzing data, which leads to loss of resolution in comparison to crystallography and SAXS is

often described as being a low-resolution technique (does not give information on atomic coordinates, instead giving an envelope of more generalized density)[60]. In preparing samples for use in SAXS or x-ray crystallography, one must obtain samples of known concentrations that are highly pure and identical, free of contaminates or aggregation, in a known buffer. Failing to do this leads to unusable data[67]. Gleaning structural information about the binding epitopes of anti-FVIII antibodies, in conjunction with their method of FVIII inhibition provides invaluable insight into the mechanics of FVIII's function, as observed in the development of the C2 domain phospholipid binding model.

Phospholipid Binding Model

The lipid binding model of FVIII has been developed and built upon since the first crystal structure of the FVIII C2 domain, published in 1999, revealed the presence of two hydrophobic beta-hairpin loops within the C2 domain that extend beyond the globular fold of the protein. These loops, which are surrounded by basic residues, were proposed to extend into the anhydrous interior of the phospholipid bilayer[68]. Since then, detailed structural investigations of the FVIII C2 domain both alone and in complex with antibodies, have continued to refine the binding model. Multiple studies have shown the two solvent-exposed hydrophobic loops to associate with the anhydrous interior of lipid bilayers (L2251/L2252 and M2199/F2200)[68,69]. In conjunction with this hydrophobic interaction is a ring of positively charged, basic residues adjacent to the solvent-exposed loops, that are thought to interact with the negatively charged phosphatidylserine (PS) on the surface of activated platelets[69]. This model of lipid binding via these hydrophobic loops is further supported by a structure of the C2 domain in complex with

human-derived classical inhibitory antibody B02C11. The CDR loops of B02C11's variable region completely segregate the hydrophobic loops of C2, resulting in a loss of lipid binding[70]. While all signs point that FVIII's binding interaction with phospholipids is driven by the hydrophobic solvent exposed loops of the C domains embedding into the lipid bilayer, the orientation of the protein during lipid binding is a bit more elusive.

The FVIII lipid binding model has been further elaborated upon thanks to epitope mapping via the crystal structure of isolated C2 ternary complex with two pathogenic antibodies, G99 and 3E6. 3E6 is a classical inhibitor (prevents lipid binding) while G99 is a non-classical inhibitor (allows lipid binding). By examining the locations of the two different, non-overlapping epitopes of these antibodies (one inhibitory to lipid binding the other having little to no effect on lipid binding) one can make extrapolations about whether these areas of the C2 domain are, or are not, involved in lipid binding. This ternary structure of C2 provided valuable insight into the orientation of the binding interactions, drawing importance away from residues previously thought to be involved in lipid binding that were found to be within the G99 epitope. In addition, the 3E6 epitope did not include the two hydrophobic loops, however, it illustrates complete loss of lipid binding by instead sequestering basic residues adjacent to these loops. This suggests that lipid binding is driven by both hydrophobic and electrostatic interactions in conjunction with one another, as opposed to the electrostatics providing a supporting role to the hydrophobic loops. By overlaying high resolution structures of C2 in complex with B02C11, 3E6 and G99 a lipid binding model was built, with the hydrophobic loops bound to B02C11 within the anhydrous lipid membrane, positively charged basic residues bound to 3E6 in an orientation that allows them to interact with the negatively charged surface of activated

platelet membranes and the residues bound to G99 facing away from the lipid membrane (Figure 9)[71].

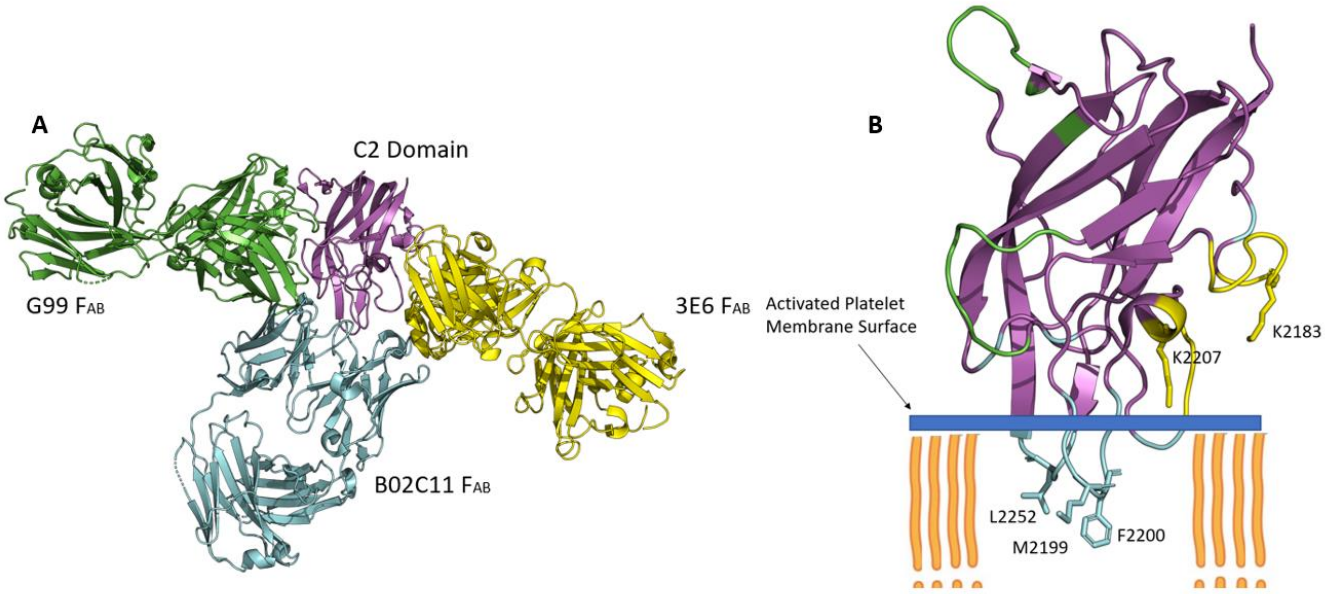

Figure 9. Inhibitor based platelet binding model of FVIII C2 domain (shown in purple). A) Anti-C2 inhibitors in complex with isolated FVIII C2 domain, alignment of classical inhibitors 3E6, yellow, and B02C11, cyan, with non-classical inhibitory G99, green (PDB #4KI5 and #1IQD). B) Hydrophobic residues make up two loops which insert the anhydrous leaflet of platelet membranes and make up the binding epitope of B02C11 shown in cyan. Basic residues interact with the negatively charged headgroups of PS made up of the binding epitope of 3E6, shown in yellow, while the binding epitope on the non-classical antibody G99 faces away from the lipid membrane interface, shown in green[76]. Key residues for 3E6 and B02C11 binding are shown as sticks and labeled. (PDB #6MF0).

Phospholipid C Domain Electrostatic Interactions

When activated, there is a recruitment of PS to the surface of platelet membranes, resulting in a negative shift in the charge on the membrane surface. Without this negative charge, FVIII has little to no affinity to phospholipids[72]. Studies have shown that FVIII specifically binds to the L-isomer of PS (OPLS), while >95% of FVIII activity is lost when the D-isomer is used (OPDS)[73]. Similarly, studies have found that the C2 domain on its own lacks this specificity

(maintains specificity for negatively charged lipids), while a C2-deleted FVIII construct, retained its specificity of OPLS binding. Beyond this, C2 was shown to have a loss of lipid binding in the presence of physiological concentration of NaCl, while full length FVIII saw a 2-fold decrease in binding affinity while retaining some binding, reflective of a loss of the C2 domain's binding affinity[64]. Examining homology modeling alongside membrane binding predictions implicate two arginine residues of the C1 and C2 domains in phospholipid binding, R2320 of the C2 and R2163 of the C1[74]. Examining C2 mutational data, the R2320T hemophilia A mutation has been shown to have only 5% activity relative to WT and is conserved across species as well as the homologous C domains of FV and Lactadherin, in addition to the FVIII C1 domain[75]. Electrostatic surface mapping illustrates that the R2320 residue has the greatest basic electrostatic potential of the C2 domain, suggesting the importance of this residue in stabilizing interactions with negatively charged phospholipids. Unfortunately, there is little mutational or assay-based data examining the C1 domain, and as such few inferences can be made about the R2163 residue. However, this residue is conserved across species and between homologous proteins. Unpublished mutational data from the Spiegel lab has shown a near complete loss of C1C2 lipid binding when the R2163 and R2320 residues are mutated to serine, validating the importance of these residues in this key interaction.

All of this implies that the binding interactions of the C2 domains hydrophobic loops acts in conjunction with electrostatic interactions between the protein and the lipid. Additionally, this indicates that the C2 domain acts in cooperation with other domains to be specifically recruited to the surface of activated platelets. While this alongside the apparent flexibility of the C2 domain and loss of lipid affinity in the presence of physiological NaCl concentrations

appears to imply that a different region of the protein (likely C1) acts to initially recruit and bind FVIIIa, followed by conformational shifts in the C2 domain to stabilize lipid binding and eventually allow for FVIIIa dissociation, the exact mechanism of lipid association and dissociation has yet to be fully understood.

Research Aims

Furthering our understanding of both the mechanism of function and mechanism of inhibition of FVIII and the key residues therein provides a blueprint when designing hemophilia A therapeutics. The goals of this study included the successful optimization of five anti-A2 inhibitor Fab fragments, the successful crystallization and collection of diffraction data for the 4A4 Fab, as well as the formation of inhibitor:ET3i complexes for use in structural study. SAXS data was successfully collected for six different inhibitor-ET3i pairings, providing insight into the binding epitopes and possible mechanisms of inhibition of anti-A2 inhibitors 4F4 and 4A4. Additional strides were made in obtaining x-ray diffraction data for the 4A4:ET3i and human derived NB2E9:C1 complexes. Beyond this, progress was made in the confirmation of proposed docking and undocking conformations of the C2 domain, by designing mutants that would lock the C1C2 construct in its undocking conformation. Four various 'disulfide' mutants were successfully purified with one of these mutants being shown to have successfully formed an additional disulfide bond when compared to the WT. Efforts are currently ongoing on both of these fronts.

Materials and Methods

Determination of C1C2 Cysteine Mutation Sites

Potential residues for cysteine mutations were identified using FVIII structural models in PyMol, PDB ID 6MF0 and 7K66. Residue pairs were chosen based on the distances between their alpha carbons in the proposed docking conformation vs. the proposed undocking confirmation of the C2 domain of FVIII. Four residue pairs were chosen that were modeled to be close enough to form a disulfide bond in the undocking confirmation, while being far enough apart in the docking confirmation to be unable to form a disulfide linkage with the hope of locking the mutant C1C2 construct in the undocking confirmation.

Transformation of FVIII C1 and C1C2 Domain Containing Plasmids

hFVIII C1C2 domain (residues 2087-2350) were ordered from Genscript in a pET32a+ vector using *BamH1* and *Xho1* restriction sites. FVIII C1C2 residues were transformed into chemically competent C3029J Shuffle K12 *E. coli* cells following New England Biolabs' high efficiency transformation protocol with the following mutations: H2031C/V2294C, T2023C/S2175C, T2023C/V2294C, T2023C/L2324C. Transformed cells were plated on agar plates containing 100 µg/mL ampicillin and grown at 30 ^{o}C for 24 hours. Single colonies were harvested from the ampicillin plates and allowed to grow in LB at 30 ^{o}C, 180 RPM for 16-18 hours. Following this growth phase cell cultures were stored at -80 ^{o}C, 20% (v/v) glycerol.

Growth, Expression, and Purification of C1 WT and Mutant C1 Constructs

Overnight cultures were grown from *E. coli* Shuffle K12 cells stocks in 10 mL LB, at 30 ^{o}C while shaking at 180 RPM and added to 1 L of 2xYT media with 40 mM $MgCl_2$ and 40 mM KCl, while maintaining 30 ^{o}C and 180 RPM until the 600 nm absorbance reached 0.6-0.8. Once the proper absorbance values were reached the temperature was adjusted to 15 ^{o}C and 200 RPM and the flasks were allowed to cool for 30 min, following which protein expression was induced via the addition of isopropyl B-D-thiogalactopyranoside (IPTG) to 500 µM and left overnight for 18-20 hours. Cells were pelleted by centrifugation at 6371x g for 10 min at 4 ^{o}C (FIBERLite F10-6x500y rotor, Thermo Fisher Scientific). Pellets were divided into 50 mL falcon tubes with pellet from 3 L of cell growth per tube and resuspended in 30-35 mL of cold Lysis buffer (300 mM NaCl, 20 mM Tris-HCl pH 7.5, 10 mM imidazole pH 8.0, 10.0% (v/v) glycerol and 0.5% (v/v) Triton X-100) 350 µL of 100 mM phenylmethylsulfonyl fluoride (PMSF) was added followed by 700 µL of 50 mg/mL lysozyme. The resuspended cell slurry was then allowed to enzymatically lysed while rotating at 15-20 RPM for 30 min at 4 ^{o}C, following which the cells were mechanically lysed using a Branson Sonifier 450 probe at power output 5 and duty cycle 50% for 30 seconds three times with a 30 second rest between each cycle. Cell debris was removed via centrifugation at 16,500 RPM for 45 min at 4 ^{o}C (FIBERLite F21- 8x50y rotor, Thermo Fisher Scientific), followed by filtration with 5 µm sterile syringe filters. Immobilized metal affinity chromatography (IMAC) was performed using TALON cobalt immobilized affinity resin (TAKARA Bio) which was equilibrated in lysis buffer, using 1 mL settled resin per 2 L cell growth. Resin was incubated with filtered lysate for 15 min rotating at 15-20 RPM at 4 ^{o}C. Resin was then re-settled in column and rinsed with 15 CV of lysis buffer, 30 CV ATP wash buffer (10 mM ATP, 50

mM HEPES pH 7.4, 300 mM KCl, 10 mM $MgCl_2$) with a pause after the first 15 CV ATP wash where the resin was resuspended on column and allowed to resettle for 10 min before finishing the wash step, 30 CV lysis buffer, 30 CV wash buffer (20 mM HEPES pH 7.4, 300 mM NaCl, 15 mM imidazole, 10% v/v glycerol), and eluted with elution buffer (20 mM MES pH 6, 300 mM NaCl, 150 mM imidazole, 10% v/v glycerol) after allowing the elution buffer to incubate on column for 10 min. Eluted protein was concentrated and dialyzed into storage buffer consisting of 20 mM HEPES, 300 mM NaCl, 10% v/v glycerol, pH 7.4-8.0 and subsequently concentrated with a 10 kDa spin filter to a concentration between 0.2-1 mg/mL and stored at -80 ^{o}C. Purity was accessed via SDS-PAGE using 12.5% bis-acrylamide gels.

Growth, Expression, and Purification of C1C2 WT and Mutant C1C2 Constructs

Overnight cultures were grown from *E. coli* Shuffle K12 cells stocks in 10 mL LB, at 30 ^{o}C while shaking at 180 RPM and added to 1 L of 2xYT with 40 mM $MgCl_2$ and 40 mM KCl, while maintaining 30 ^{o}C and 180 RPM until an OD_{600} of 0.4-0.6. Once the proper absorbance values were reached the temperature was adjusted to 15 ^{o}C and 200 RPM and the flasks were allowed to cool for ~30 min, following which protein expression was induced via the addition of isopropyl B-D-thiogalactopyranoside (IPTG) to 500 µM and left overnight for 18-20 hours. Pellets were divided into 50 mL falcon tubes with pellet from 3 L of cell growth per tube and resuspended in 30-35 mL of cold Lysis buffer 350 µL of 100 mM PMSF was added followed by 700 µL of 50 mg/mL lysozyme. The resuspended cell slurry was then allowed to enzymatically lysed while rotating at 15-20 RPM for 30 min at 4 ^{o}C, following which the cells were mechanically lysed using a Branson Sonifier 450 probe at power output 5 and duty cycle 50%

for 30 seconds three times with a 30 second rest between each cycle. Cell debris was removed via centrifugation at 16,500 RPM for 45 min at 4 ^{o}C (FIBERLite F21- 8x50y rotor, Thermo Fisher Scientific), followed by filtration with 5 µm sterile syringe filters.

The filtered sample was then loaded onto a Capto HisTrap HP 5 mL column attached to a fast protein liquid chromatography (FPLC) device (AKTA prime Plus manufactured by GE Healthcare Life Sciences) equilibrated in lysis buffer at 2 mL/min. The column then underwent several wash steps all at a flow rate of 3 mL/min. First, buffer A (500 mM NaCl, 20 mM imidazole, 50 mM HEPES, pH 7.4) until the UV and conductance baselined, ~50 mL. Next the column was washed with 50 mL of freshly prepared ATP wash buffer (300 mM KCl, 50 mM HEPES pH 7.4, 20 mM $MgCl_2$, 10 mM ATP) flow was stopped for 10 minutes following which an additional 50 mL of ATP wash buffer was flown over the column. Flow was then switched back to buffer A and ran until the UV and conductance baselined, ~70 mL. Flow was then switched to 92% buffer A, 8% buffer B (500 mM NaCl, 500mM imidazole, 50 mM HEPES pH 7.4) and ran until UV and conductance baselined. Finally, a gradient elution was conducted over the course of 100 mL going from 8-100% buffer B and collected in 4 mL fractions. Each fraction was collected, and purity determined via SDS-PAGE. Fractions with >95% purity were dialyzed into storage buffer consisting of 20 mM HEPES, 500 mM NaCl, 10% v/v glycerol, pH 7.4-8.0 and stored at -80 °C.

TEV Cleavage

Plasmids ordered from Genscript contained a tobacco Etch Virus (TEV) cleavage sequence between the C1 or C1C2 domains and a penta-His tag and Thioredoxin solubility tag.

Cleavage reactions were conducted by adding 25 µL of 1 mg/mL TEV per 2 mg of protein with the reactions being conducted at 30 °C 150 RPM for ~3.5 hours. Following which, the sample was collected, and the cleaved C domains were purified via IMAC using ~1-2 mL Talon resin. The sample was incubated with the talon resin for ~30 minutes and the flow through was collected, purity accessed via SDS-PAGE and the sample stored at -80 °C.

The C1C2 H2031C/V2294C was additionally purified on size exclusion chromatography (SEC) (S75, Cytiva Life Sciences) equilibrated in HBS with 450 mM NaCl. The fractions were accessed for purity via SDS-PAGE and pure fractions were pooled.

Mass Spectrometry

Molecular weights of WT and mutant C1C2 constructs were verified following an LC-ESI-MS workflow using an Agilent 6545XT AdvanceBio Q-TOF system in conjunction with an Agilent 1290 HPLC system. Prior to use, a mass calibration check was conducted with masses ranging from 118.08 to 2721.89 Da. Prior to loading samples, the system was conditioned with buffer A (H_2O 0.1% formic acid) at a flow rate of 0.3 mL/min, following which a full gradient elution was conducted with no sample injection as follows; 0.0-1.0 min 90% buffer A 10% buffer B (100% MeCN), 1.0-9.0 min linear gradient of 10-90% buffer B, 9.0-11.0 min 90% buffer B, 11.0-11.1 min linear gradient of 90-10% buffer B, 11.1-15.0 min 10% buffer B, all while collecting MS data. Following this 'no injection' sample was injected into the HPLC and the same gradient elution procedure was followed for each subsequent sample. Once loaded onto the system samples were first desalted and then separated via the gradient elution using a Phenomenex Aeris 3.6 mM WIDEPORE C4 200 Å column (100x2.1 mm). After all samples were run a second 'no

injection' sample was conducted. Peptides were ionized via electrospray ionization (ESI) and loaded onto the Q-TOF. The ESI source was set as follows; gas temp 350 °C, drying gas 9 l/min, nebulizer 35 psi, sheath gas temp 325 °C, sheath gas flow 8 l/min, VCap 4500 V, fragmentor 225 V, skimmer 70 V. Ion charge ladders were deconvoluted using Agilent MassHunter BioConfirm software (ver. 10.0) with a mass range of 30,000-60,000 Da.

In addition to running unmodified samples, various modified samples were also run over the same LC-ESI-MS workflow, while following the same gradient elution and data work-up procedure. Both WT C1C2 and each of the disulfide mutants were subjected to the following modifications and run on the MS: reduced with dithiothreitol (DTT), reduced with DTT then alkylated with iodoacetamide (IAA). Additionally, a reducing fine screen was conducted by treating the H2031C/V2294C mutant with a range of DTT concentrations; 0.05 mM to 5 mM.

Mammalian Cell Growth

In a sterile hood, 9 mL of Hybridoma Medium E (MedE) from STEM Cell Technologies (CAT#03805) was placed into a sterile 15 mL falcon tube. Hybridoma cell stocks stored in liquid nitrogen at ~1 million cells/mL in CryoStor® CS10 from STEM Cell Technologies (CAT#07959) were thawed in a 37 ^{o}C water bath for 2 min. Thawed cell stocks were added to the 9mL MedE aliquot, and gently inverted to mix. Cells were pelleted by centrifugation at 1000 RPM for 5 min. The supernatant was discarded and the hybridoma cells gently resuspended in 2 mL of MedE, this 2 mL suspension was transferred to a T-75 flask containing 15-25 mL of MedE. The flask was loosely sealed and stored in a sterile water bath incubator at 5% CO_2 and 37 ^{o}C. Cells

were monitored over a 10-day growth period considering cell adherence to the flask, percent confluence and color of media. Once cells reached 50% or higher confluence the MedE was disposed of and 5 mL of Animal Origin Free (AOF) media from STEM Cell Technologies (CAT#03835) was added to the flask. Cells were sloughed off the flask by gently slapping and scraping the inside of the flask with a sterile serological pipet. Cell density and viability were assessed by combining 200 µL of Trypan Blue solution (0.4%) (CAT#T8154) with 50 µL of sloughed cell media and placing 20 µL of this mixture onto an INCYTO C-Chip hemocytometer (DHC-N01), counting the number of viable cells within a 1 mm^2 grid, and extrapolating the cell count for the cell slurry. The remaining AOF cell slurry was then collected, and the cells passaged into new T-75 flasks containing 15-25 mL of AOF or MedE at a rate of ~1 million cells per MedE flask and ~2 million cells per AOF flask. Following passaging, the original MedE flask would either be discarded or recycled by adding an additional 15-25 mL of MedE and allowing the remaining adherent cells to repeat the 10-day growth period.

Antibody Collection from AOF Media

While the hybridoma cells express anti-fVIII antibodies throughout the growth process, the collection of these antibodies was done in AOF media. Following passaging into AOF containing T-75 flasks, the cells were left to grow and express for ~10 days. Following this expression period, the media was harvested and spun at 1000 rpm for 5 minutes at room temperature, the supernatant collected, and 20% sodium azide added to the supernatant to a final concentration of 0.1%. This antibody containing media was stored for under 5 days at 4 °C or at -80 °C for long term storage.

Antibody Purification with Protein A Resin

The collected antibody containing media was diluted at a ratio of 1:1 with antibody binding/wash buffer (0.1 M HEPES, 0.15 M NaCl pH 8). The diluted media was run over 2-3 mL of Protein A resin in a disposable gravity column at a flow rate of 1 mL/min or less, and the FT collected. The column was then washed with 5 CV of antibody binding/wash buffer and the wash collected. Elution was conducted with 15 mL of 0.2 M glycine pH 2.0-3.0 and collected into a falcon tube containing 1.5 mL of 1.5 M Tris-HCl pH 8.8 and 1.5 mL of 5 M NaCl. Purity was accessed via SDS-PAGE, and stored at -80 °C.

Antibody Cleavage with Immobilized Papain

The antibody sample was buffer exchanged into sample buffer (10 mM EDTA, 20 mM Na phosphate, pH 7) and ~150 µL of immobilized papain slurry (CAT#20341) equilibrated in digestion buffer (10 mM EDTA, 20 mM NaP, 20 mM cysteine-HCl, pH 7) was added per mg of antibody, with the digestion buffer being prepared immediately prior to use. The cleavage reaction was conducted overnight in a shaking water bath at 37 °C and 180 RPM. Following cleavage, the papain resin was removed from the sample, and the sample was diluted with ~1/5th the sample volume PBS. ~300 µL of protein A slurry (CAT#20333) equilibrated in PBS was added to the sample and placed on a rocker for 1-2 hours. Following incubation with protein A the protein A resin was removed from the sample and Fab purity and cleavage success was accessed via SDS-PAGE. The Fab sample was dialyzed into PBS and stored at -80 °C.

Antibody-FVIII Complex Formation

Two 'types' of antibody-FVIII complexes were formed; full length ET3i, obtained from our collaborators Dr. Christopher Doering and Dr. Gabriela Denning, in complex with one or two murine derived anti-FVIII Fab in complex with full length ET3i, and human derived anti-C1 NB2E9 Fab, obtained as an monoclonal antibody (mAb) from our collaborators Dr. Carmen Coxon, with cleaved WT FVIII C1 domain. When forming the anti-A2-ET3i complexes both the Fabs and ET3i were buffer exchanged into 1x HBS with 5% v/v glycerol. These proteins were mixed at a molar ratio of 1:1.2 ET3i:Fab or 1:1.2:1.2 ET3i:Fab:Fab and let sit on ice for ~30 min. The complexes were then spun in a 10 kDa spin filter to concentrations between 1-2 mg/mL and stored at -80 °C. When forming the NB2E9-C1 complex the proteins were buffer exchanged into 1x HBS with 5% v/v glycerol. These proteins were mixed at a ratio of 1:2 Fab:C1 and let sit on ice for ~30 min. The complex was then spun in a 30 kDa spin filter to a concentration of 1.2 mg/mL and stored at -80 °C.

Antibody Complex SEC

Anti-A2-ET3i complexes used for small-angle X-ray scattering (SAXS) were purified via SEC (S200, GE Healthcare) equilibrated in HBS. Peaks were collected and purity tested by SDS-PAGE gel, the complex and excess Fab were collected separately and stored at -80 °C.

Small Angle X-Ray Scattering

The following binary and tertiary ET3i-antibody complexes, purified via SEC, were sent to the Advanced Light Source (ALS) Berkeley Center for Structural Biology (BCSB) Sibyls

Beamline 12.3.1 (Berkeley, Ca) and SAXS data collected for each ; 1-D4:ET3i, 1-D4:G99:ET3i, 2-101:ET3i, 2-101:G99:ET3i, 4F4:ET3i, 4F4:G99:ET3i, 4A4:ET3i, 4A4:G99:ET3i, 4C7:ET3i, 4C7:G99:ET3i. This work was conducted at the ALS, a national user facility operated by Lawrence Berkeley National Laboratory on behalf of the Department of Energy, Office of Basic Energy Sciences, through the Integrated Diffraction Analysis Technologies (IDAT) program, supported by DOE Office of Biological and Environmental Research. Additional support comes from the National Institute of Health project ALS-ENABLE (P30 GM124169) and a High-End Instrumentation Grant S10OD018483.

Crystallography

The NB2E9 Fab-ET3i complex was sent to the Hauptman-Woodward Medical Research Institute National High-Throughput Crystallization Center (HWI) for hanging drop crystal screening of 1,536 different chemical conditions. The crystallization screening at the National Crystallization Center at HWI was supported through NIH grant R24GM141256. A variety of fine screens were designed and plated based on the HWI screen. These fine screens yielded crystals, which were looped and sent to the ALS BCSB beamline 5.0.1 (Berkeley, Ca), however none of these crystals diffracted.

The NB2E9:C1 complex was then sent to HWI for hanging drop crystal screening of 1,536 various chemical conditions. The crystallization screening at the National Crystallization Center at HWI was supported through NIH grant R24GM141256. From this a variety of fine screens were designed and plated. These fine screens have yielded crystals, some of which have been

looped and sent to the ALS BCSB beamline 5.0.1, however none of these crystals showed diffraction.

The 4A4, 4F4, and 4C7 FabS were screened in house using the following screens from Hampton Research; PEG/Ion Screen™ (HR2-126), PEGRx 2 Screen™ (HR2-084), Crystal Screen HT™ (HR2-110). A variety of fine screens were designed and plated, based on the initial screening, which yielded crystals that were looped and sent to the ALS BCSB beamline 5.0.1. A lone 4A4 crystal grown via hanging drop vapor diffusion in 0.2 M calcium chloride dihydrate and 20% PEG 3350 and cryoprotected with a 1:1 addition of 0.2 M calcium chloride dihydrate, and 40% PEG 3350, yielded usable diffraction data. Crystal growth occurred over the course of approximately one week at room temperature. Based on the successful crystallization and diffraction of the 4A4 Fab, the 4A4:ET3i complex was constructed and sent to HWI for hanging drop crystal screening of 1,536 different chemical conditions. A variety of fine screens were designed and plated based on the HWI screen.

Nanodisc Preparation

MSP1D1 grown and purified by previous students was cleaved with TEV by adding 25 µL of 1 mg/mL TEV per 2 mg of MSP1D1 and allowed to react for ~3.5 hours at 30 °C 150 RPM. 1,2-dioleoyl-sn-glycero-3-phosphocholine (DOPC) and 1,2-dioleoyl-sn-glycero-3-phospho-L-serine (DOPS), stored in chloroform were mixed in a glass tube at a molar ratio of 80:20, and the chloroform dried overnight in a fume hood. Lipids were solubilized with 100 µL 1x HBS containing 26 mM sodium chocolate. Lipids were solubilized by hot running tap water (~40-50 °C), vortexing, and water bath sonication until the lipid solution turned clear. MSP1D1 were

added to a final molar ratio of 1:200 MSP:lipid, additional sodium cholate was added to a final concentration of 50 mM and additionally HBS was added to a final volume of 500 µL. This mixture was incubated for one hour at 37 °C, following which 500 µL of Biobeads equilibrated in HBS were added and the mixture sat overnight, mixing, at 4 °C. Samples were purified via size exclusion chromatography (S200, GE Healthcare) equilibrated in HBS. Peaks were collected and nanodiscs were tested by assessing binding to WT C1C2 via biolayer interferometry (BLI). Fractions were pooled based on C1C2 binding curves, and stored at 4 °C.

Biolayer Interferometry

Biolayer interferometry (BLI) was used to confirm binding between antibody-protein and protein-lipid interactions. BLI was conducted with a Pall ForteBio® BLITz instrument alongside the BLITz Pro software. BLI was conducted in five different steps: initial baseline, loading, baseline, association, dissociation. First, a BLI tip was attached to the instrument and 200 µL of HBS were added to a LiteSafe® Black Microtube, the BLI run was then started, and the tip submerged in the black microtube for the initial baseline. Following this the tip is moved into 4 µL of sample (with affinity for the tip in question) for the loading step, following this the tip was resubmerged in the black microtube for the baseline step. The tip, bound to the target protein, was then placed into 4 µL of the second sample and the two samples were allowed to interact for the association step, following which the tip was placed back into the black microtube for the dissociation step. In addition to testing samples a negative control was measured during each BLI run, which follows the same procedure as a regular BLI run, except instead of placing the tip into the sample with affinity for the tip during the loading step the tip

was placed in 4 µL of HBS.

Two different tips were used when conducting BLI: Octet® HIS1K Biosensors and Octet® ProA Biosensors. The HS1K Biosensors were used to bind to C1, C2, and C1C2 constructs to assess binding with lipid vesicles and lipid nanodisc, the ProA Biosensors were used to bind to IgG to assess binding with Et3i, C1, C2, and C1C2 constructs.

Results

FVIII Mutant Design

ET3i structures of the proposed docking and undocking conformations were used to identify residues to mutate to cysteine. Residues were chosen such that the distance between the alpha carbons was close enough to form a disulfide linkage in the 'undocking' conformation while being too far apart in the 'docking' conformation. Disulfide bonds can form when the alpha carbons of two cysteines are within ~8 Å [77]. As such, the parameters for picking residues were that in the undocking conformation the two residues' alpha carbons were within ~8 Å with an increase in distance between alpha carbons in the docking conformation. Four residue pairs were identified and ordered (Figure 10).

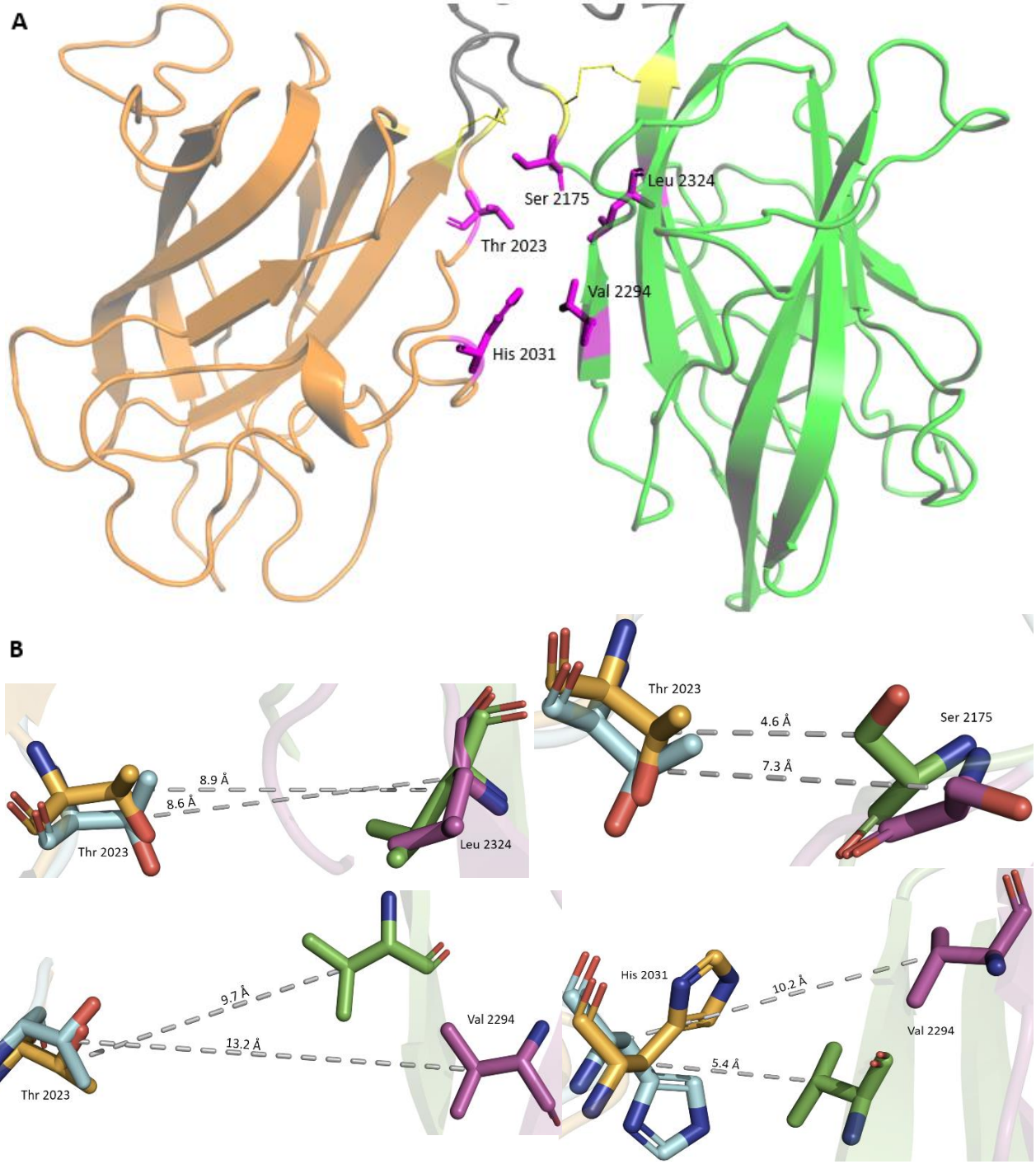

Figure 10. C1C2 disulfide mutant design. A) C1C2 in the proposed undocking conformation, C1 in orange, C2 in green, the residues of interest are colored in purple and labeled, the two native disulfide bonds of C1C2 are shown in yellow. B) Mutation residue pairs showing the distance between alpha carbons in the proposed undocking, C1 orange and C2 green, and proposed docking, C1 cyan C2 purple, conformations. Nitrogen is shown in blue, and oxygen shown in red. Residues and bond distances are labeled. (PDB# 6MF0).

FVIII C domain expression and purification

Wild type hC1C2, hC1 and their various mutants were successfully transformed into SHuffle K12 *E. coli* cells to assist in proper disulfide bond formation. The SHuffle K12 cell line yielded successful expression of soluble WT C1C2, C1 as well as the various mutants. Following IMAC, samples consistently contained a 70 kDa contaminant that was able to be removed on a protein-by-protein basis. The WT C1 and C1C2 were able to be purified with a typical IMAC purification scheme with the addition of ATP washes to remove the contaminant (Figure 11), with yields of approximately 4 mg/L and 1 mg/L pure protein, respectively (Table 3). This proved to be unsuccessful when purifying C1 and C1C2 mutants. C1C2 mutants (R2163S/R2320S, T2023C/V2294C, T2023C/L2324C, T2023C, S2175C, H2031C/V2294C) and the C1 mutant (R2163S) were able to be purified with a gradient elution on FPLC using a nickel affinity column with large imidazole and ATP wash steps (Figure 11). Notably, the same purification protocol was successful in purifying all the various mutants. Mutants R2163S/R2320S and R2163S were both used in lipid binding studies as described by Peters, 2021[83].

Table 3. Approximate C1 and C1C2 Construct Expression Levels and Purification Scheme

Protein	Average Yield of Pure Protein	Purification Scheme
WT C1	4 mg/L	IMAC, additional clean-up as needed
WT C1C2	1 mg/L	IMAC, additional clean-up as needed
C1 Mutant	~0.9 mg/L	FPLC Ni column, or successive IMAC
C1C2 Mutants	~0.333 mg/L	FPLC Ni column

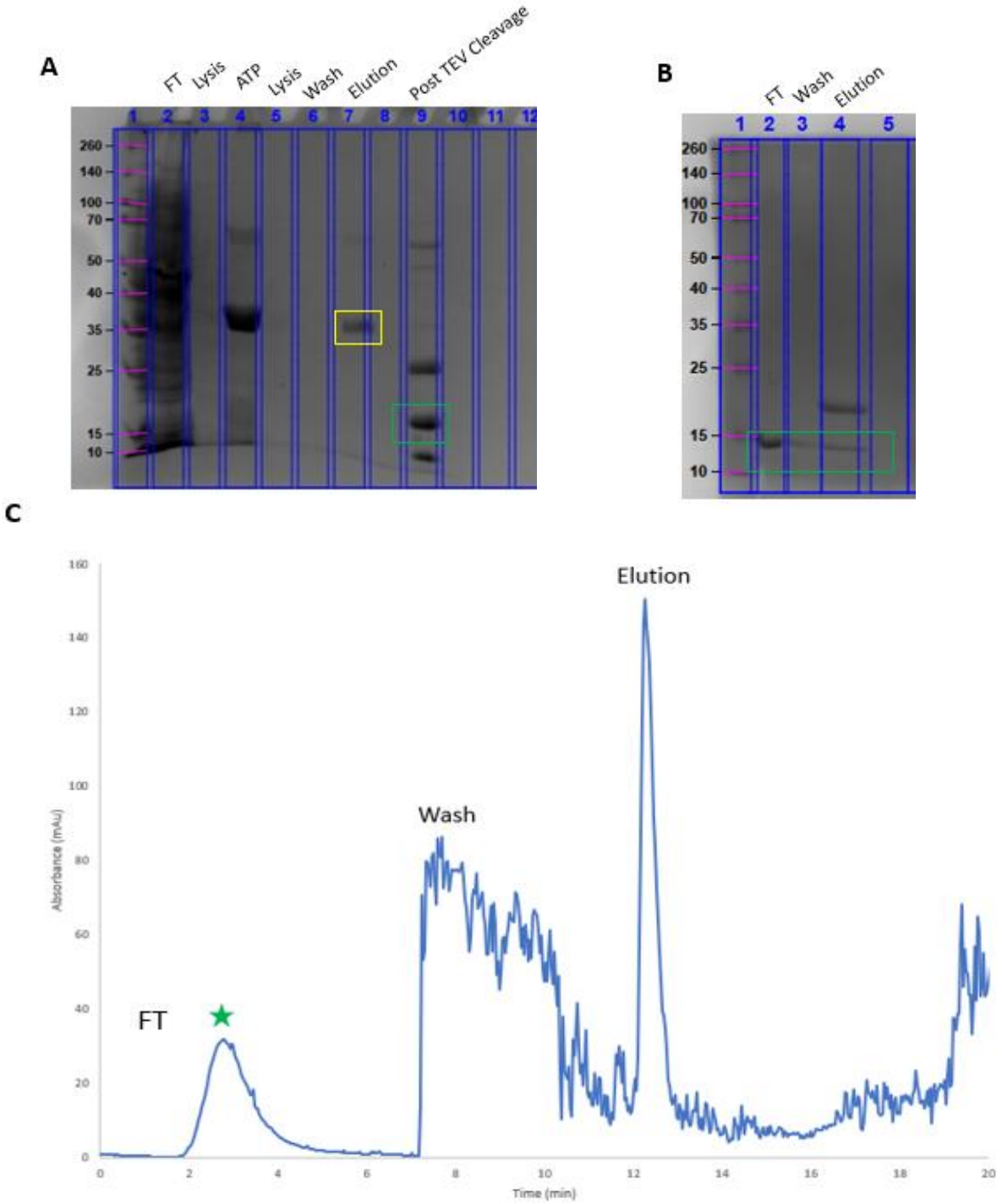

Figure 11. C1 WT initial purification, cleavage, and subsequent purification. A) SDS-PAGE gel image of a typical C1 Talon IMAC purification, and post TEV cleavage sample. All the different lanes are labeled, with un-cleaved C1 boxed in yellow, and cleaved C1 boxed in green. B) SDS-PAGE gel image of cleaved C1 on a Q-column, lanes are labeled and cleaved C1 is boxed in green. C) Q-column chromatogram, each of the different purification steps are labeled, with pure cleaved C1 denoted with a green star.

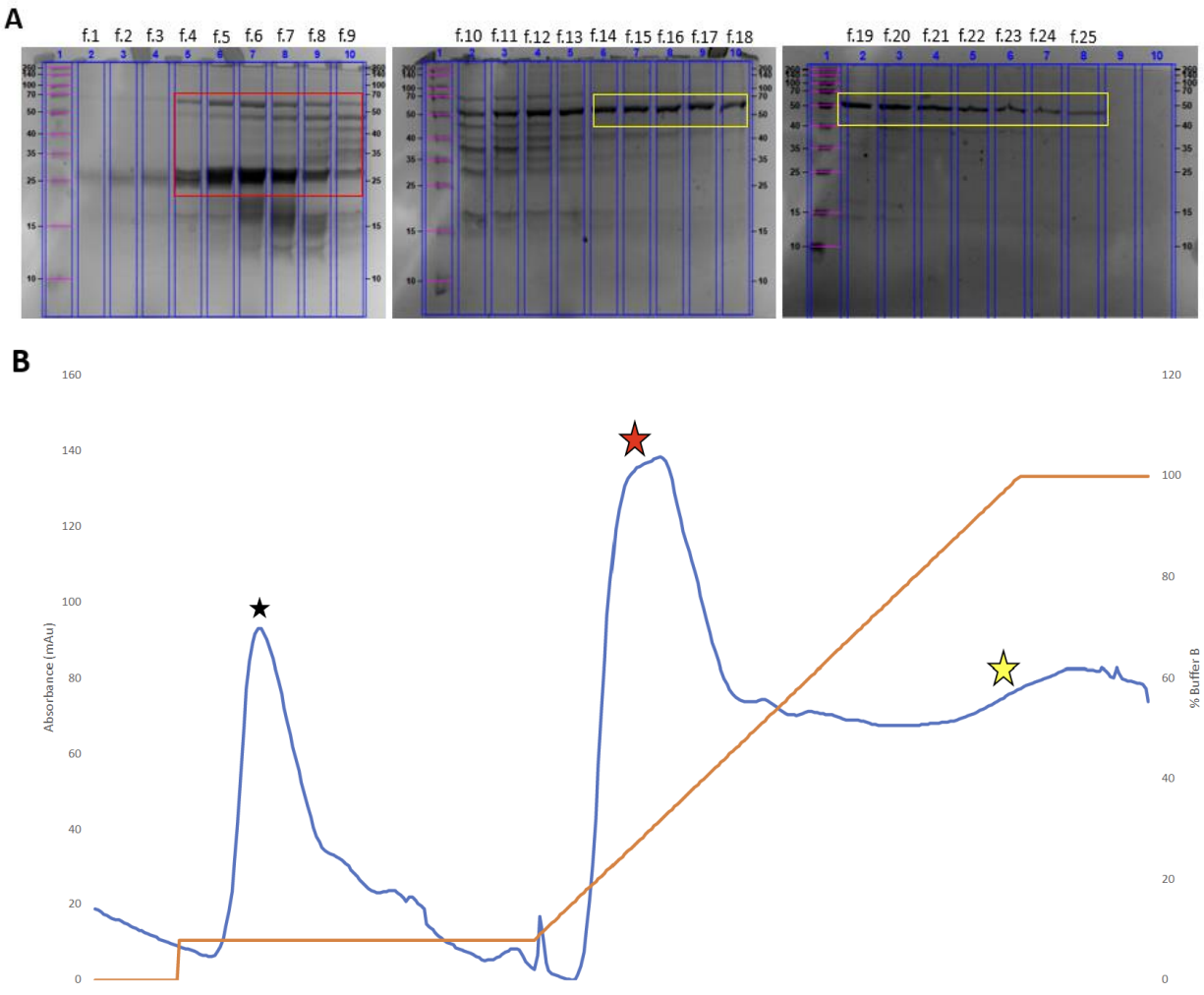

Figure 12. C1C2 disulfide mutant purification. A) SDS-PAGE gel image of C1C2 T2023C, S2175C FPLC Ni-NTA purification, with fraction number X labeled as f. X. Non-pure samples are boxed in red and pure samples are boxed in yellow, corresponding to the red and yellow stars on the chromatograph. B) Ni-NTA chromatogram of C1C2 T2023C, S2175C purification, absorbance shown by the blue curve, and % buffer B shown by the orange curve. The black star shows the end of the ATP wash and the elution of the 70 kDa contaminant, the red star shows the beginning of elution off the column, matching the fractions boxed in red on the gel image, and the yellow star shows the elution of the purified sample, corresponding to the yellow boxed fractions on the gel image. See appendix figures 2-4 for purification of the other three disulfide mutants.

C1 WT TEV Cleavage

Recombinant WT C1 contained a TEV cleavage site as previous attempts to cleave the protein ran into difficulties when using enterokinase. TEV cleavage was optimized such that cleavages occurred over the course of ~3 hours at 37 ◦C. Minimal protein precipitation was observed when compared to overnight cleavages at 4 ◦C. Purification of the cleaved C1 was successful in removing all contaminants, either through IMAC purification or IEC. Using talon resin the cleaved HIS-TRX tag and HIS-TEV were bound to the column as the untagged C1 flowed through. This, however, would not always be enough to purify the sample, in which case purification using a Q column was conducted at a pH of ~7. C1 has a basic theoretical pI of 9.96, and so at a pH of around 7 it would have a positive charge removing affinity for the column. On the other hand, both TEV and TRX have theoretical pIs of less than 6 giving them a negative charge at this pH and a high affinity for the column.

Disulfide Mutants

During the COVID pandemic there were numerous supply chain issues, including ATP, so while the C1C2 mutants T2023C/V2294C, T2023C/L2324C, T2023C, S2175C, H2031C/V2294C (disulfide mutants) were able to be successfully purified on FPLC with an ATP wash, alternative methods were attempted. These all proved to be unsuccessful in purifying the target protein to the same degree as the ATP method, and so “PEAK ATP®”, a work-out supplement advertised as “Pure ATP” was bought from amazon and used in lieu of laboratory grade ATP. This ATP replacement showed excellent promise and was able to remove the 70 kDa contaminant to a

comparable degree on IMAC wash steps, however it was not fully pursued as laboratory grade ATP became available.

The identity of the disulfide mutants was validated and the constructs assessed for proper folding via binding kinetics to anti-C1 and anti-C2 inhibitors via BLI. The molecular weight of the formed constructs were further validated via mass spectrometry (MS). This proved to be successful in confirming the MW of 3 of the 4 disulfide mutants as well as WT (Table 4).

To test if the desired disulfide bond had formed, MS data was collected for both reduced and non-reduced samples of the disulfide mutants. As the formation of a disulfide bond reduces the molecular weight of a protein by 2 Da[78], the number of disulfide bonds within a protein can be determined by comparing the weights of reduced and non-reduced samples. This successfully illustrated the formation of a new disulfide bond for C1C2 mutant H2031C/V2294C, via an 8 Da shift between the reduced and non-reduced samples (Figure 13). The H2031C/V2294C was then further purified on SEC in preparation for conducting lipid binding assays (Figure 14). Initial reducing and alkylating conditions were tested for the H2031C/V2294C mutant. Reduction was successful, however the expected molecular weight shift that would be seen via successful alkylation with IAA was not observed.

Table 4. C1C2 Disulfide Mutant's Molecular Weights

Mutant	Theoretical Molecular Weight (kDa)	Molecular Weight Found on MS (kDa)
T2023C/V2294C	54.446	54.3-54.5
T2023C/L2324C	54.432	N/A
T2023C, S2175C	54.458	54.366
H2031C/V2294C	54.410	54.280
WT	54.440	53.307

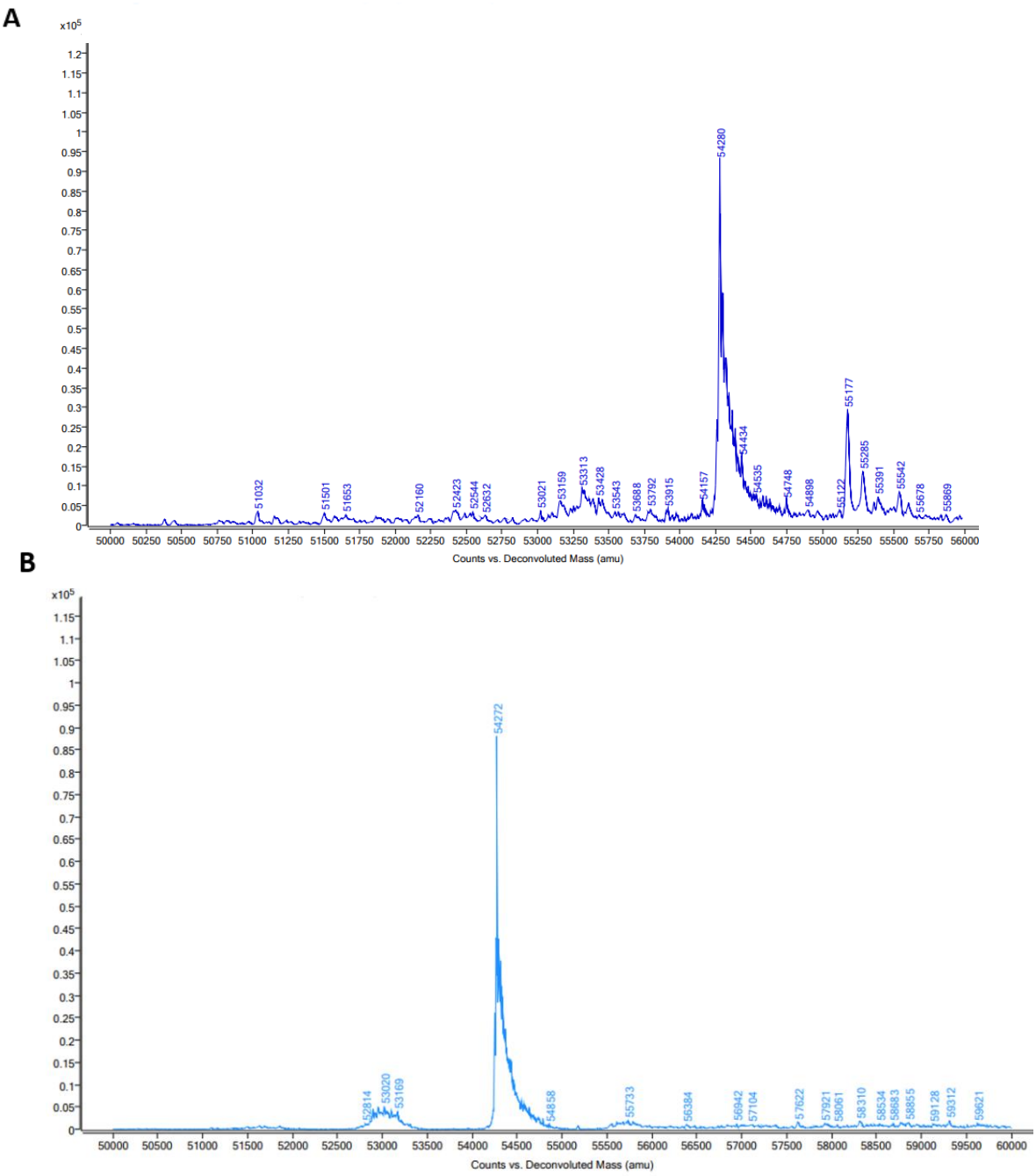

Figure 13. Mass chromatogram for C1C2 H2031C/V2294C under reducing and non-reducing conditions. A) Reduced sample, showing a mass of 54,280 Da B) Non-reduced sample, showing a mass of 54,272 Da, 8 Da smaller than the reduced sample.

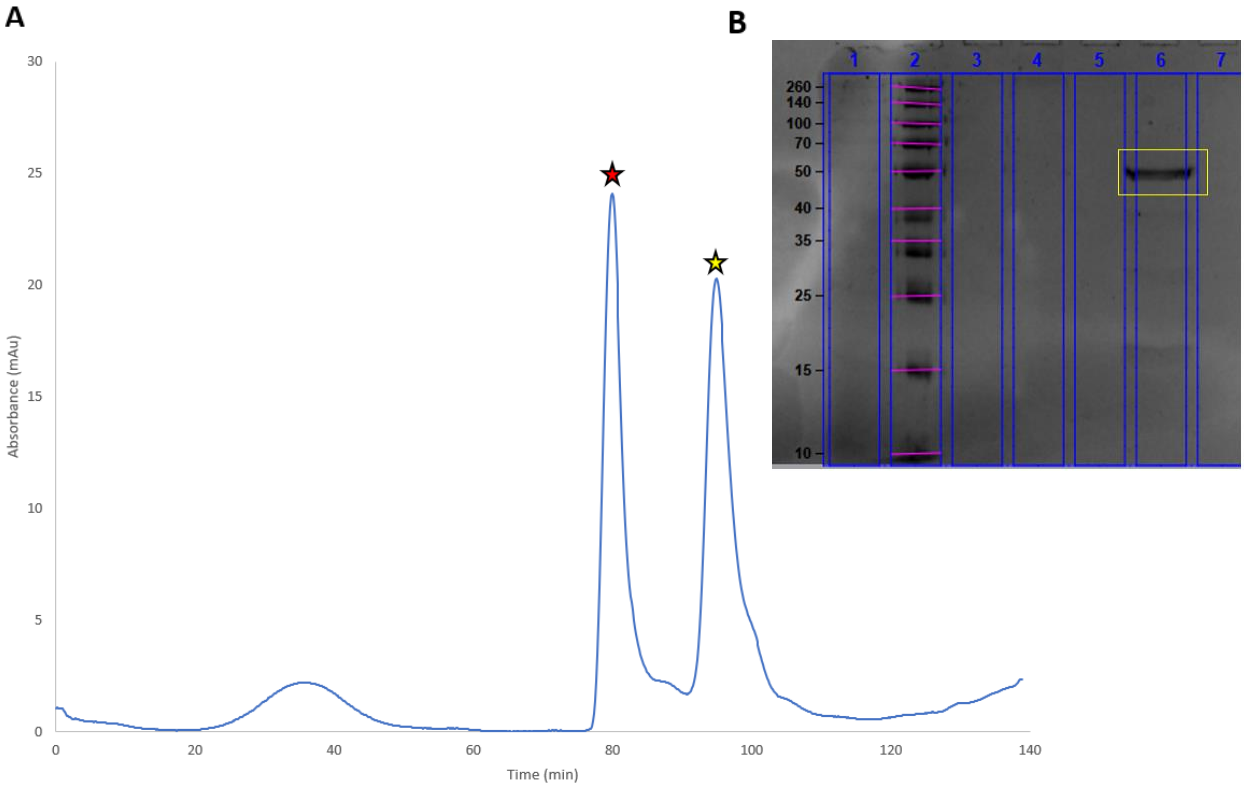

Figure 14. C1C2 H2031C/V2294C SEC purification. A) SEC chromatogram, two peaks were eluted from the column, the first peak, denoted with a red star, was ran on a gel, but no bands were detected (the 260/280 ratio for this peak was found to be ~3 suggesting that this peak is a DNA contaminant), while the second peak denoted with a yellow star, was eluted at the expected volume for the C1C2 construct. B) SDS-PAGE gel of the two SEC peaks, the C1C2 H2031C/V2294C collected from the second peak is boxed in yellow.

Antibody Growth and Purification

Antibody growth and purification was attempted with two anti-C1 mAbs (B136, M6143) and five anti-A2 mAbs (4A4, 4F4, 1-D4, 2-101, 4C7). Hybridoma cells expressing the murine derived B136 and M6143 were successfully cultured, however there was little to no expression observed. This is likely due to improper storage of the hybridoma cells at -80 ^{c}C rather than in liquid nitrogen, as well as irregular temperatures due to freezer electrical issues. The five anti-A2 mAbs were successfully cultured and expressed and are now kept in proper storage

conditions. Cell culture begins in Medium E, a fetal bovine serum-based media and contains a variety of bovine proteins, including antibodies. These additional proteins make purification of the target mAb next to impossible. To combat this, cells are passaged into Animal Origin Free (AOF) media, which allows for easy purification from the media. Cell growth and expression were tracked by consumption of nutrients via an acidic byproduct which results in a color shift in the indicator containing media, as well as via visual cell adherence.

An additional shortage we encountered due to supply chain issues was T-75 cell growth flasks. As such flask recycling was developed to continue antibody production. Here, either AOF or MedE flasks underwent cell sloughing and these cells were removed followed by the addition of additional media. This practice was found to be successful, however not a replacement for regular cycling of growth flasks.

Upon mAb harvesting the media was diluted with buffer and purified with protein A resin, which binds to $IgG2_{ak}$ antibodies. Antibodies were then successfully cleaved via papain and optimized to occur overnight at 37 °C. The subsequent Fab purification was also consistently successful (Figure 15).

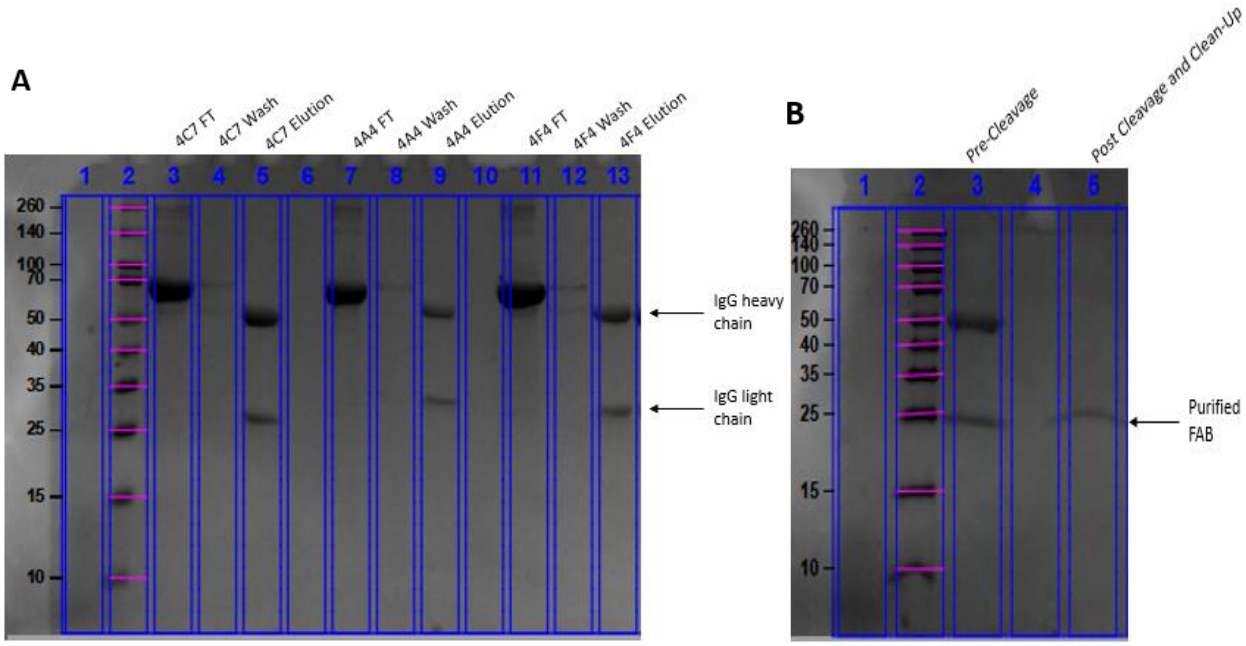

Figure 15. Antibody purification and cleavage. A) SDS-PAGE gel image showing flow through (FT) wash and elution steps in the purification of 4C7, 4A4, and 4F4, IgG heavy and light chains are marked by black arrows. B) SDS-PAGE gel image showing a pre-IgG cleavage sample vs. a cleaved and purified Fab sample

SAXS

Formation of ET3i in complex with anti-A2 inhibitory antibodies and subsequent purification via SEC was successful. Usable SAXS data was collected at the ALS beamline and processed for the ET3i:G99, ET3i:G99:4F4, ET3i:G99:4A4 complexes by Dr. Kenny Childers. The known ET3i:G99 crystal structure (PDB #7KBT) was superimposed into the generated SAXS envelopes to examine validity of the envelopes and identify the location of 4A4 and 4F4 within the envelope (Figure 16). These envelopes illustrate the presence of additional density outside of ET3i at the expected position for G99, as well as additional densities protruding from the A2 domain in the 4A4 and 4F4 containing constructs.

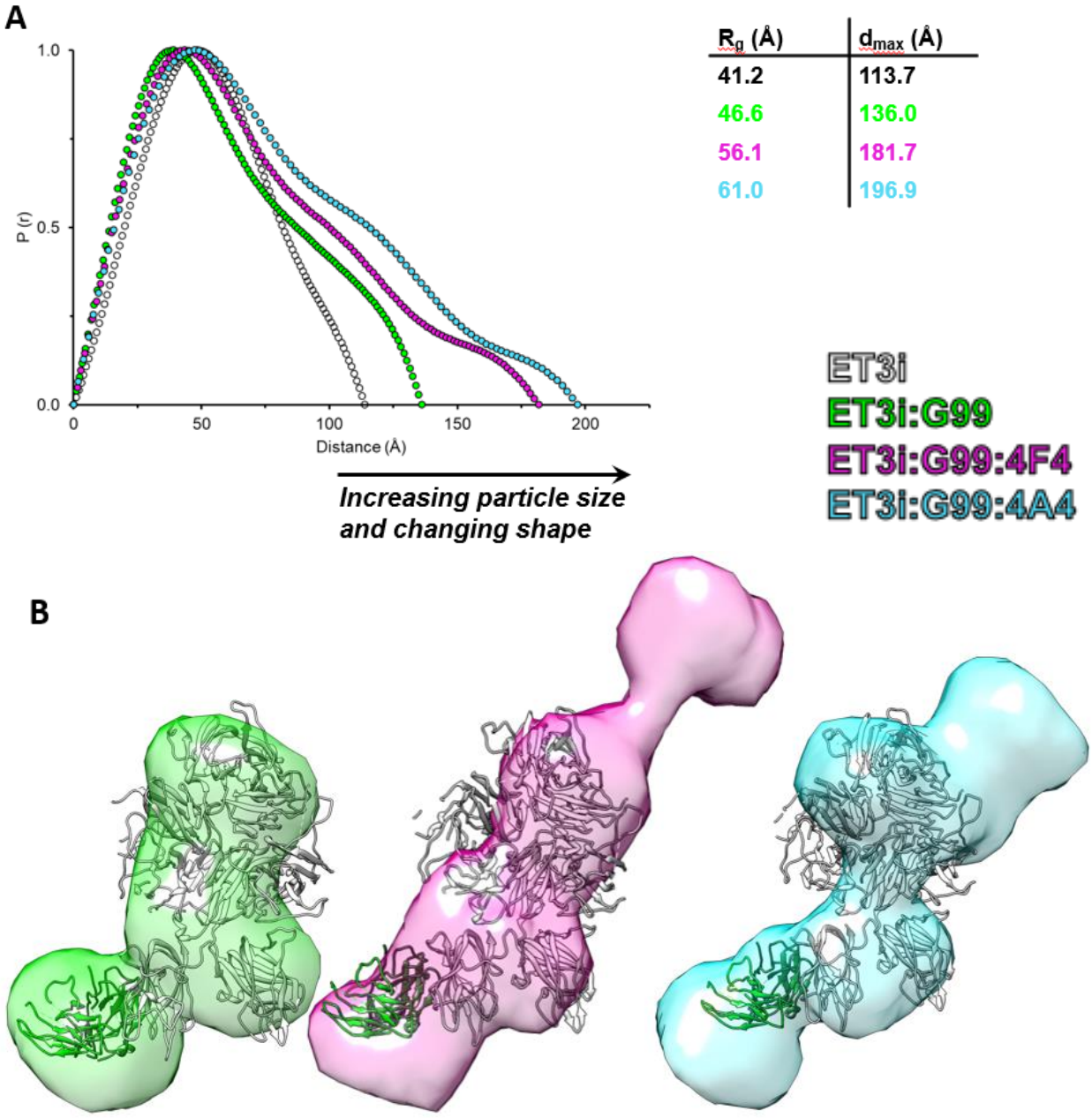

Figure 16. SAXS data generated for ET3i, and the ET3i:G99, ET3i:G99:4F4, ET3i:G99:4A4 complexes. A) Pair distance distribution function (P(r)), illustrating the probability of any two points A and B to be X distance apart, as well as the radius of gyration (R_g) and maximum distance between atoms (d_{max}) used when calculating the P(r) for the ET3i:G99 (green), ET3i:G99:4F4 (magenta), and ET3i:G99:4A4 (blue) complexes B) Images of the ET3i:G99 crystal structure superimposed on the generated SAXS envelopes for the ET3i:G99 (green), ET3i:G99:4F4 (magenta), and ET3i:G99:4A4 (blue) complexes. (Data work-up done by Dr. Kenny Childers).

Crystallography

Anti-A2 inhibitor Fabs of 4A4, 4F4, and 4C7 were screened in house using Hampton Research screens. These generated crystal hits were further pursued with fine screening, and crystals were looped and sent for data collection at the ALS beamline. Lower quality diffraction was detected for two 4F4 crystals, and seven 4A4 crystals of varying conditions. A single 4A4 crystal generated higher quality diffraction with a 2.08 Å resolution (Figure 17). This crystal was grown via hanging drop vapor diffusion in 0.2 M calcium chloride dihydrate and 20% PEG 3350. As this illustrated the 4A4 Fab's ability to produce high quality crystals, the ET3i:4A4 alongside the C1:NB2E9 complex were sent to the Hauptman-Woodward Institute for a 1536 condition crystal screen. A variety of fine screens were designed based on these large screens for both complexes. At the time of writing C1:NB2E9 crystals have been looped and sent to the ALS beamline, but failed to diffract, and the ET3i:4A4 conditions have just begun to be plated.

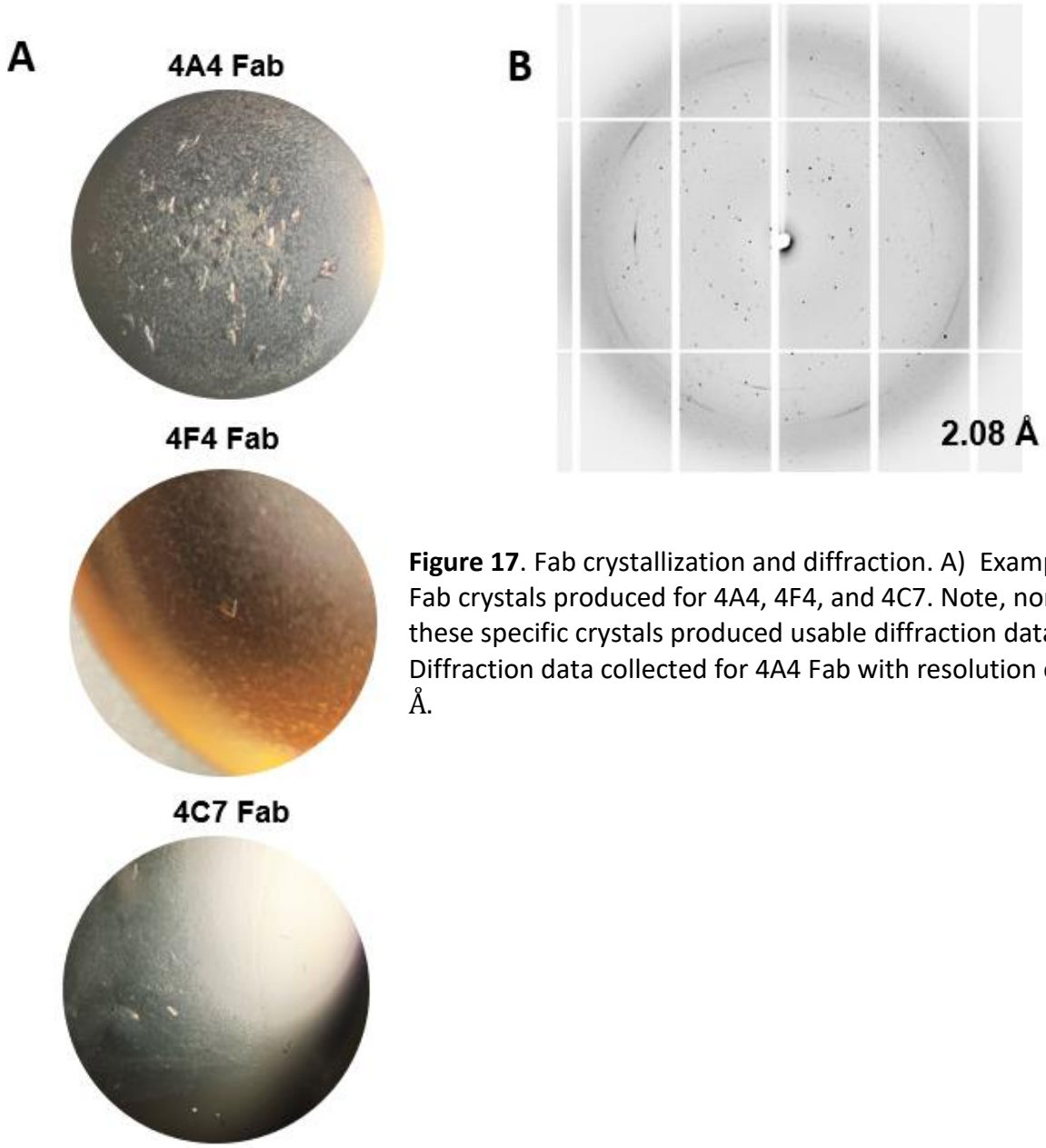

Figure 17. Fab crystallization and diffraction. A) Examples of Fab crystals produced for 4A4, 4F4, and 4C7. Note, none of these specific crystals produced usable diffraction data. B) Diffraction data collected for 4A4 Fab with resolution of 2.08 Å.

Nanodisc Prep

MSP1D1 80:20 (PC:PS) nanodiscs were successfully constructed following protocols designed by previous graduate students. The formed nanodiscs were then further purified via

SEC, and the various fractions' binding affinities for C1C2 WT were determined and the fractions pooled based on similar levels of binding affinity (Figure 17). Pooled fractions were stored at 4 °C, for future use in lipid binding studies.

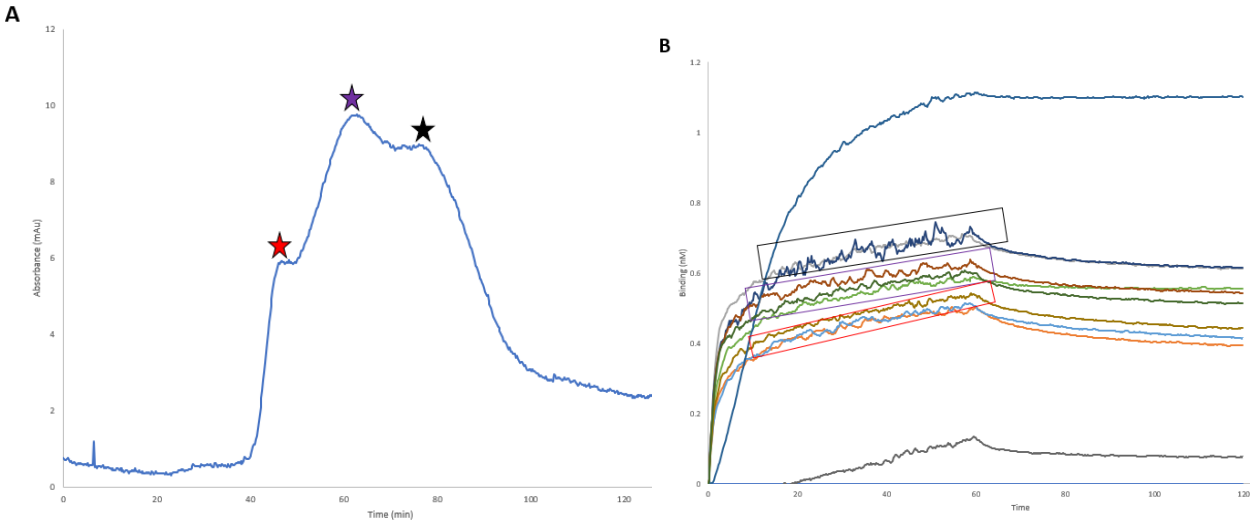

Figure 17. Nanodisc purification. A) SEC of MSP1D1 80:20 (PC:PS) nanodiscs. Three separate peaks were collected and accessed for binding to C1C2 WT via BLI, denoted by the red, purple, and black stars. B) BLI binding curves of the collected fractions and C1C2 WT. Fractions were pooled based on having similar levels of binding, denoted by the black, purple, and red boxes, which also correspond to the elution peaks of the respective fractions (matched by color of star and box).

Biolayer Interferometry

Initial BLI binding data was collected and used to confirm the identity and fold of the disulfide mutants, by collecting binding data between the mutants and the anti-C1 NB2E9 and anti-C2 BO2C11 inhibitors. Each of the disulfide mutants illustrated binding to both NB2E9 and BO2C11 to a similar degree as the WT sample tested (figure 18). Initial BLI binding data was collected and used to verify the identity of the anti-A2 antibodies by showing binding to ET3i. Each of the five anti-A2 inhibitors illustrated binding to ET3i, with varying degrees of binding

with 1-D4 and 4A4 showing the highest binding affinities followed by 4F4, and 2-101, with 4C7 having little to no additional binding in comparison to the blank (figure 19). As neither of these experiments were conducted with varying protein concentration nor in triplicate, exact binding capacities are unable to be determined. Regardless of not determining exact binding, binding affinity was confirmed.

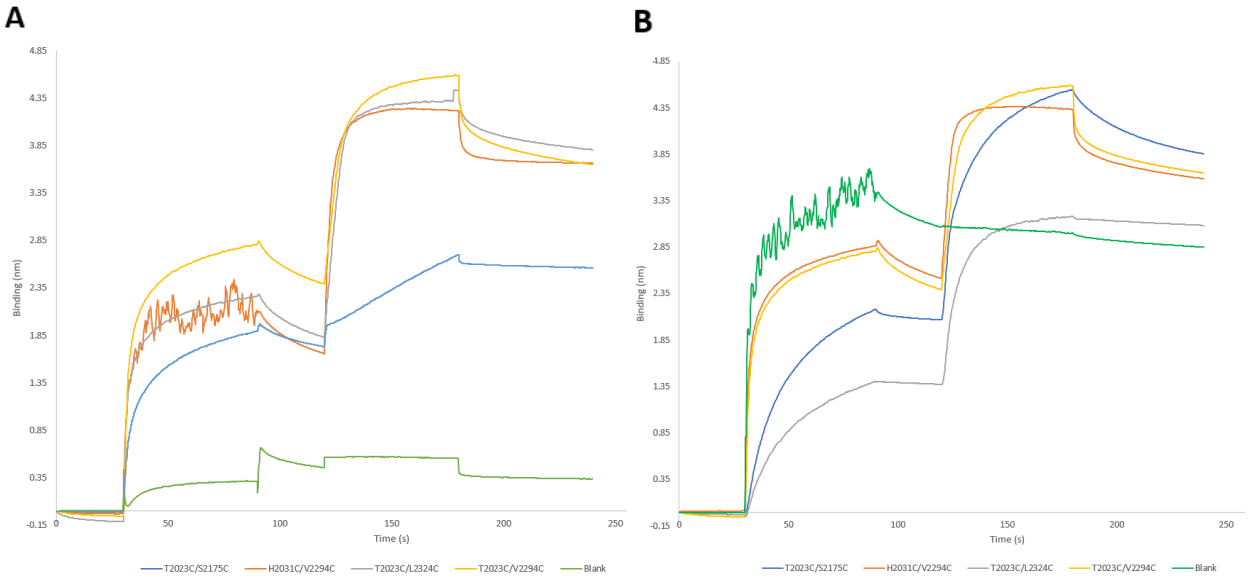

Figure 18. C1C2 disulfide mutants' antibody test binding. A) C1C2 disulfide mutants' test binding to anti-C2 inhibitor NB2C11, with mutations and negative control labeled on the chart. B) disulfide mutants' test binding to anti-C1 inhibitor NB2E9, with mutations and negative control labeled on the chart with the same color scheme as A.

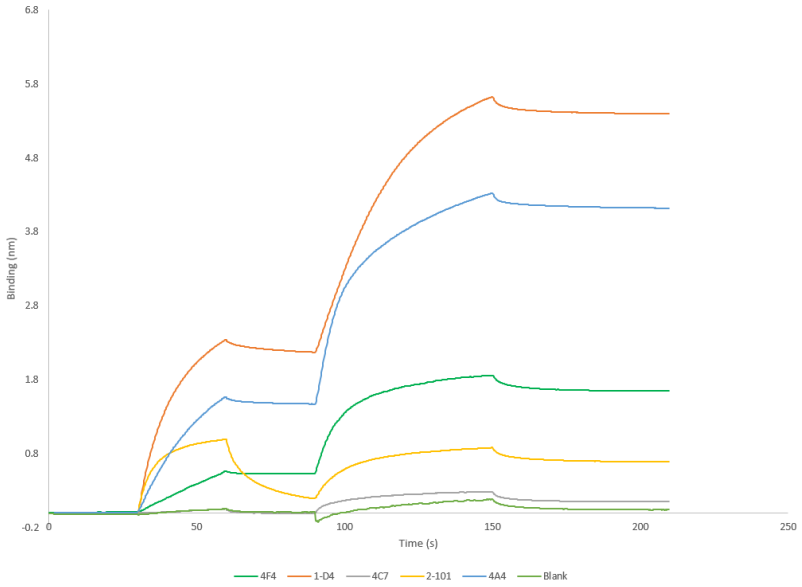

Figure 19. All five anti-A2 inhibitors' test binding to ET3i to confirm identity and binding to FVIII, with inhibitors and negative control labeled on the chart.

Discussion

FVIII's C domains facilitate binding to the surface of activated platelet membranes, allowing for the formation of the tenase complex. Binding models proposed have illustrated the importance of both electrostatic interactions between positively charged basic residues of FVIII and negatively charged PS headgroups, as well as the hydrophobic solvent exposed loops of the C1 and C2 domains embedding into the anhydrous inner membrane coordinating and stabilizing this lipid binding interaction. The data generated to build these binding models has focused primarily on the C2 domain; however, there are implications for the importance of the C1 domain. Notably, the C2 domain appears to have a great degree of flexibility, having been shown to rotate ~35-45^{o} about a central set of residues. This flexibility is thought to perhaps illustrate a docking and undocking conformation of the C2 domain[45]. This flexibility alongside the lone C2 constructs lack of PS specificity, while a C2 deleted FVIII construct retains PS

specificity indicates the possibility of the C1 domain coordinating the initial binding interaction followed by a conformational shift of the C2 domain causing it to swing down and stabilize the lipid binding interaction. Additionally, the C2 domain sees a near complete loss of lipid binding at physiological concentrations of NaCl, while full length FVIII retains binding approximately equivalent to the C2 deleted construct[64]. This illustrates the importance of electrostatic interactions in facilitating C2 lipid binding and shows that there are differences between the C1 and C2 domains' mechanism of binding as well as possible regulation mechanisms.

Previous attempts to express soluble C1C2 and C1 constructs have been attempted by other labs but were unsuccessful[79]. Through the addition of a Trx solubility tag and expression in a modified SHuffle T7 vector that has been optimized to promote slow protein expression alongside proper folding in disulfide-containing proteins and native disulfide bond formation[80] has proved to be successful in producing constructs that are properly folded while being retained in the soluble fraction. Despite this, purification of any C1-containing construct is plagued by a persistent 70 kDa contaminant, not seen in C2 constructs, that was unable to be removed using typical wash buffers of more than 50 column volumes. This contaminant is thought to be a chaperone (HSP70) that is naturally expressed in *E. coli*, which recognizes and binds to the large, solvent exposed hydrophobic region (~1400 $Å^2$) of C1. Additionally, the three-fold larger hydrophobic region of C1 vs. C2 may help to explain poor solubility seen for C1 when compared to C2. The mechanism of chaperone release is driven by the phosphorylation of the chaperone by ATP, as well as interaction with one K^+ and two Mg^{2+} ions. As such, $MgCl_2$ and KCl were added to the growth media to help prevent initial binding of sample to the chaperone, and a purification protocol was developed which included an ATP wash step (also

containing $MgCl_2$ and KCl). This modified expression and purification protocol proved to be extremely successful at removing this troublesome contamination, notably being shown to work for five different C1C2 mutants and three different C1 mutants. This is of note, to further our understanding of FVIII's lipid binding mechanism, studies will need to investigate the C1 domain. The C2 domain has thus far been the primary protein of study for FVIII's lipid interactions, this is in part due to the ease of expression, solubility, and stability of this protein in comparison to the C1 domain. Our expression and purification protocol's seemingly universal application to mutant C1 containing constructs illustrates a methodology that allows for mutational studies at a wide variety of residues. This shows promise moving forward in our understanding of C1's role in the lipid binding mechanism.

The flexibility of the C2 domain points to the possibility of a docking and undocking conformation. Four different C1C2 mutant constructs were designed and ordered such that if a disulfide bond were to form between the mutation sites, it would lock C2 in its proposed undocking conformation. Each of the four mutants were able to be successfully expressed and purified. The identity and proper fold of each of the constructs was confirmed via binding to anti-C1 and anti-C2 inhibitors via BLI, and molecular weight was confirmed on MS. The WT C1C2-Trx construct contains 3 native disulfide bonds (2 within C1C2 and 1 in Trx). Formation of a disulfide bond can be observed by a loss of 2 Da per bond in the overall mass of the construct. The formation of a 4th disulfide bond, not seen in WT, was observed in the H2031C/V2294C C1C2 mutant by an 8 Da shift between reduced and non-reduced samples illustrating success in the formation of the designed disulfide bond. The mutant in question is an excellent candidate to lock C1C2 in its undocking conformation, as the distance between the alpha carbons of

H2031 and V2294 shifts from 5.4 Å to 10.2 Å from the undocking to docking conformations. Moving forward with this project will require validating the location of this new disulfide bond, determining reduction conditions that selectively break only this bond, and conducting lipid binding assays to determine if there is a loss of binding when the designed disulfide bond is present.

FVIII is an essential cofactor within the blood coagulation cascade, with those who have a deficiency of functional FVIII having a condition known as hemophilia A. The most common complication of hemophilia A treatment is the development of inhibiting antibodies that bind to exogenous FVIII rendering it non-functional. The two most immunogenic domains of FVIII are the C2 and A2 domains, with additional implications for the C1 domain. While there has been extensive investigation of the immunogenic effects on the C2 domain, there has yet to be a structure of an anti-A2 inhibitor bound to FVIII. There also has yet to be a structure of FVIII's C1 domain in complex with a human derived antibody, which would provide validity to the previous data collected using murine derived inhibitors when working with human models. Unfortunately, despite obtaining diffraction data with a 2.08 Å resolution, the structure of the 4A4 Fab still needs to be solved as our lab has yet to receive the full sequence. Regardless, the successful crystallization and diffraction of the 4A4 Fab is a promising start to being able to obtain x-ray crystallographic data for the ET3i:4A4 complex. In addition, the successful formation of the C1:human-derived-NB2E9 complex has allowed for a large-scale crystal screening, with fine screens ongoing. As of writing there have been crystals looped and treated with x-rays for the NB2E9 complex, however, there has yet to be any usable diffraction data.

Beyond x-ray crystallography, SAXS data was collected for ET3i bound to anti-A2 antibodies 4A4 and 4F4, as well as anti-C2 G99, whose x-ray crystal structure bound to ET3i has previously been determined. The generated SAXS envelopes for the ET3i:G99, ET3i:G99:4A4, ET3i:G99:4F4 complexes matched previous structural data of the ET3i:G99 complex, with additional density protruding from the A2 domain in the 4A4 and 4F4 containing complexes. While the 4F4 epitope has yet to be mapped, superimposing the 4F4 and 4A4 SAXS envelopes supports a partial overlap of the 4A4 and 4F4 epitopes (Figure 20). The 4A4 binding epitope was previously determined to be between residues Asp403-His444[55], however the exact binding, and thereby method of FVIII inhibition, have yet to be determined. Of the 403-444 FVIII sequence there are two regions, 403-422 and 427-444, which are solvent exposed with residues 423-426 completely buried within the A2 domain. Within the superimposed image of the two SAXS envelopes and the ET3i:G99 structure the additional density presumed to be the 4A4 Fab appears to completely cover residues 403-422

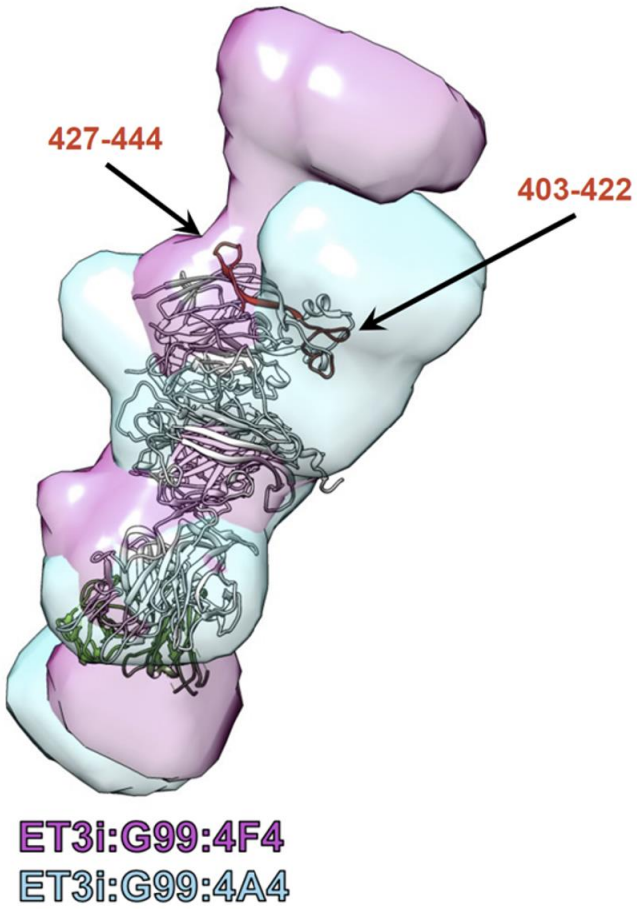

Figure 20. Superimposition of ET3i:G99:4F4, shown in purple, and ET3i:G99:4A4, shown in blue, and ET3i:G99 crystal structure, with solvent exposed residues in the proposed 4A4 binding epitope labeled in red. (Data work up done by Dr. Kenny Childers).

with some coverage of residues 427-444, while the 4F4 Fab appears to not cover residues 403-422 with some coverage within residues 427-444 (Figure 20). Previous work has highlighted the possibility of FVIII anti-A2 inhibitors blocking a potential FX binding site corresponding to residues 400-409, resulting in loss of function in the tenase complex[81]. This may point to 4A4's method of inhibition, as well as explain why 4A4 is 121 times more immunogenic than 4F4 (Table 2), as it appears that 4F4's binding epitope does not cover the 400-409 region. Again, this data will contain greater insight once we have the sequences of both 4A4 and 4F4 alongside additional structural data of the 4F4 Fab and both of the inhibitors in complex with ET3i.

Conclusions and Future Work

Hemophilia A is an X-linked recessive condition that affects 1 in 5,000 male births, most commonly treated via venous injection of recombinant FVIII to act as a replacement for the patients endogenous FVIII. Approximately 60-70% of patients are categorized as severe, requiring frequent injections to stay on top of bleeding episodes. About a third of these severe cases develop inhibiting antibodies during treatment which bind to the exogenous FVIII, sterically hindering key binding partners from being able to bind to FVIII, thereby rendering it non-functional. Looking forward in the development of FVIII therapeutics there are two main considerations; minimizing the immunogenic response in patients, while maintaining proper protein function. Gaining structural data of FVIII in complex with inhibitory antibodies provides invaluable insight into the binding epitopes and thereby inhibitory mechanisms of these antibodies. Knowing the key residues involved in inhibitor binding interactions may give way to

designing therapeutics that are able to lower inhibitor binding capacity and thereby inhibition of the therapeutic. To this extent continued efforts to obtain the first structure of FVIII in complex with an anti-A2 inhibitor are ongoing, as well as obtaining the first structure of FVIII in complex with a human-derived-anti-C1 inhibitor. Beyond identifying key residues involved in inhibitor binding, structural data would be able to provide insight into inhibitor mechanism, which can be used to extrapolate FVIII functional mechanisms, as seen in the development of the current lipid binding model. Understanding FVIII's mechanisms of function and the key motifs therein, sets the stage for the needed pieces to construct a functional FVIII therapeutic.

With this in mind, efforts to confirm that the FVIII C2 domain's flexibility corresponds to a lipid docking and undocking conformation are ongoing. The next steps for this project first require the validation of the location of the 4th disulfide bond observed in C1C2 mutant H2031C/V2294C in order to show that it is in fact the designed disulfide bond. This could be accomplished via simply sequencing the protein on a mass spectrometer, however due to the relative high number of disulfide bonds present in the protein the data collection and work-up might become too messy and complicated. Secondly, reducing conditions must be found such that the two native disulfide bonds of C1C2 remain intact, while the non-native, designed disulfide bond is broken. By combining this step alongside the first could prove to be a much simpler task, by sequencing the protein after first alkylating the protein, to 'mark' any free thiols, followed by reduction of the protein with varying reducing agents at differing concentrations, followed by alkylation with a different alkylating agent of differing mass than the first to separately 'mark' newly exposed thiols. By doing this one could observe which cysteines make up the 4 disulfide bonds present in the protein, as well as compare which bonds

are broken under varying reducing conditions. Thirdly, the lipid binding capacity of the proposed docking and undocking conformations must be collected and compared. To do this lipid binding affinity could be determined via BLI or lipid sedimentation assays using both the protein treated with the proper reducing conditions to solely break the designed disulfide bond, as well as a non-reduced protein sample.

Works Cited

1. Gale, A. J. Continuing Education Course #2: Current Understanding of Hemostasis. Toxicologic Pathology 39, (2011).

2. Davie, E. W. & Ratnoff, O. D. Waterfall Sequence for Intrinsic Blood Clotting. Science 145, (1964).

3. Witmer, C. & Young, G. Factor VIII inhibitors in hemophilia A: rationale and latest evidence. Therapeutic Advances in Hematology 4, (2013).

4. Gale, A. J. Continuing Education Course #2: Current Understanding of Hemostasis. Toxicologic Pathology 39, (2011).

5. Davie, E. W. & Ratnoff, O. D. Waterfall Sequence for Intrinsic Blood Clotting. Science 145, (1964).

6. Davie, E. W. & Ratnoff, O. D. Waterfall Sequence for Intrinsic Blood Clotting. Science 145, (1964).

7. Jackson, S. P. The growing complexity of platelet aggregation. Blood 109, (2007).

8. Ruggeri, Z. M. The role of von Willebrand factor in thrombus formation. Thrombosis Research 120, (2007).

9. Varga-Szabo, D., Pleines, I. & Nieswandt, B. Cell Adhesion Mechanisms in Platelets. Arteriosclerosis, Thrombosis, and Vascular Biology 28, (2008).

10. Peyvandi, F., Garagiola, I. & Baronciani, L. Role of von Willebrand factor in the haemostasis. Blood transfusion = Trasfusione del sangue 9 Suppl 2, (2011).

11. Nieswandt, B. Glycoprotein VI but not alpha2beta1 integrin is essential for platelet interaction with collagen. The EMBO Journal 20, (2001).

12. Luo, B.-H. & Springer, T. A. Integrin structures and conformational signaling. Current Opinion in Cell Biology 18, (2006).

13. O'Donnell, V. B., Murphy, R. C. & Watson, S. P. Platelet Lipidomics. Circulation Research 114, (2014).

14. Smith, S. A. The cell-based model of coagulation. Journal of Veterinary Emergency and Critical Care 19, (2009).

15. Smith, S. A. The cell-based model of coagulation. Journal of Veterinary Emergency and Critical Care 19, (2009).

16. Hedner, U. Recombinant activated factor VII as a universal haemostatic agent. Blood coagulation & fibrinolysis : an international journal in haemostasis and thrombosis 9 Suppl 1, (1998).

17. Smith, S. A. The cell-based model of coagulation. Journal of Veterinary Emergency and Critical Care 19, (2009).

18. Butenas, S. Tissue Factor Structure and Function. Scientifica 2012, (2012).

19. Smith, S. A. The cell-based model of coagulation. Journal of Veterinary Emergency and Critical Care 19, (2009).

20. Hoffman, M. Remodeling the Blood Coagulation Cascade. Journal of Thrombosis and Thrombolysis 16, (2003).

21. Kanaide, H. & Shainoff, J. R. Cross-linking of fibrinogen and fibrin by fibrin-stablizing factor (factor XIIIa). The Journal of laboratory and clinical medicine 85, (1975).

22. Naito, K. & Fujikawa, K. Activation of human blood coagulation factor XI independent of factor XII. Factor XI is activated by thrombin and factor XIa in the presence of negatively charged surfaces. The Journal of biological chemistry 266, (1991).

23. Gailani, D. Activation of Factor IX by Factor XIa. Trends in Cardiovascular Medicine 10, (2000).

24. Smith, S. A. & Morrissey, J. H. Interactions Between Platelets and the Coagulation System. in Platelets (Elsevier, 2019). doi:10.1016/B978-0-12-813456-6.00021-7.

25. Simmons, M. A. Factor Xa. in xPharm: The Comprehensive Pharmacology Reference (Elsevier, 2007). doi:10.1016/B978-008055232-3.61736-2.

26. Carcao, M., Moorehead, P. & Lillicrap, D. Hemophilia A and B. in Hematology (Elsevier, 2018). doi:10.1016/B978-0-323-35762-3.00135-9.

27. Lenting, P. J., van Mourik, J. A. & Mertens, K. The Life Cycle of Coagulation Factor VIII in View of Its Structure and Function. Blood 92, (1998).

28. Mazurkiewicz-Pisarek, A., Płucienniczak, G., Ciach, T. & Płucienniczak, A. The factor VIII protein and its function. Acta Biochimica Polonica 63, (2016).

29. TERRAUBE, V., O'DONNELL, J. S. & JENKINS, P. v. Factor VIII and von Willebrand factor interaction: biological, clinical and therapeutic importance. Haemophilia 16, (2010).

30. Panteleev, M. A., Ananyeva, N. M., Greco, N. J., Ataullakhanov, F. I. & Saenko, E. L. Factor VIIIa regulates substrate delivery to the intrinsic factor X-activating complex. FEBS Journal 273, (2006).

31. TERRAUBE, V., O'DONNELL, J. S. & JENKINS, P. v. Factor VIII and von Willebrand factor interaction: biological, clinical and therapeutic importance. Haemophilia 16, (2010).

32. Jardim, L. L., Chaves, D. G. & Rezende, S. M. Development of inhibitors in hemophilia A: An illustrated review. Research and Practice in Thrombosis and Haemostasis 4, (2020).

33. Hemophilia. Cleveland Clinic (2021).

34. Yousphi, A. S., Bakhtiar, A., Cheema, M. A., Nasim, S. & Ullah, W. Acquired Hemophilia A: A Rare but Potentially Fatal Bleeding Disorder. Cureus (2019) doi:10.7759/cureus.5442.

35. Coppola, A. Treatment of hemophilia: a review of current advances and ongoing issues. Journal of Blood Medicine (2010) doi:10.2147/JBM.S6885.

36. Leah Lawrence. The High Price of Hemophilia. American Society of Hematology (2020).

37. Treatment of Hemophilia. Centers of Disease Control and Prevention (2020).

38. Jardim, L. L., Chaves, D. G. & Rezende, S. M. Development of inhibitors in hemophilia A: An illustrated review. Research and Practice in Thrombosis and Haemostasis 4, (2020).

39. Specialised Commissioning Team. Clinical Commissioning Policy 16042/P. (2016).

40. Jardim, L. L., Chaves, D. G. & Rezende, S. M. Development of inhibitors in hemophilia A: An illustrated review. Research and Practice in Thrombosis and Haemostasis 4, (2020).

41. Su, J. et al. The Immune Tolerance Induction Factor Utilizations and Costs for the Management of Male Hemophilia-a Patients Who Developed Inhibitors. Blood 128, (2016).

42. Jardim, L. L., Chaves, D. G. & Rezende, S. M. Development of inhibitors in hemophilia A: An illustrated review. Research and Practice in Thrombosis and Haemostasis 4, (2020).

43. Mannucci, P. & Franchini, M. Porcine recombinant factor VIII: an additional weapon to handle anti-factor VIII antibodies. Blood Transfusions 15, 365–368 (2016).

44. Lollar, P., Parker, E. T. & Fay, P. J. Coagulant properties of hybrid human/porcine factor VIII molecules. Journal of Biological Chemistry 267, (1992).

45. Smith, I. W. et al. The 3.2 Å structure of a bioengineered variant of blood coagulation factor <scp>VIII</scp> indicates two conformations of the C2 domain. Journal of Thrombosis and Haemostasis 18, (2020).

46. Vidarsson, G., Dekkers, G. & Rispens, T. IgG Subclasses and Allotypes: From Structure to Effector Functions. Frontiers in Immunology 5, (2014).

47. Janeway, C. A. How the immune system protects the host from infection. Microbes and Infection 3, (2001).

48. Turner, V. B cell activation and the germinal centre response. British Society for Immunology (2021).

49. Witmer, C. & Young, G. Factor VIII inhibitors in hemophilia A: rationale and latest evidence. Therapeutic Advances in Hematology 4, (2013).

50. Lollar, P. et al. Inhibition of human factor VIIIa by anti-A2 subunit antibodies. Journal of Clinical Investigation 93, (1994).

51. Saint-Remy, J.-M. R., Lacroix-Desmazes, S. & Oldenburg, J. Inhibitors in haemophilia: pathophysiology. Haemophilia 10, (2004).

52. Fulcher, C., Lechner, K. & de Graaf Mahoney, S. Immunoblot analysis shows changes in factor VIII inhibitor chain specificity in factor VIII inhibitor patients over time. Blood 72, (1988).

53. Kruse-Jarres, R. & Leissinger, C. A. Acquired Coagulation Disorders Caused by Inhibitors. in Consultative Hemostasis and Thrombosis (Elsevier, 2013). doi:10.1016/B978-1-4557-2296-9.00006-3.

54. Peerschke, E. I. B., Castellone, D. D., Ledford-Kraemer, M., van Cott, E. M. & Meijer, P. Laboratory Assessment of Factor VIII Inhibitor Titer. American Journal of Clinical Pathology 131, (2009).

55. Coxon, C. H. et al. Characterisation and application of recombinant FVIII-neutralising antibodies from haemophilia A inhibitor patients. British Journal of Haematology 193, (2021).

56. Eubanks, J. et al. A subset of high-titer anti–factor VIII A2 domain antibodies is responsive to treatment with factor VIII. Blood 127, (2016).

57. Smyth, M. S. & Martin, J. H. x ray crystallography. Molecular pathology : MP 53, (2000).

58. McPherson, A. & Gavira, J. A. Introduction to protein crystallization. Acta Crystallographica Section F Structural Biology Communications 70, (2014).

59. Gish, J. S. et al. Structure of blood coagulation factor VIII in complex with an anti–C1 domain pathogenic antibody inhibitor. Blood 137, (2021).

60. Narayanan, T. et al. A multipurpose instrument for time-resolved ultra-small-angle and coherent X-ray scattering. Journal of Applied Crystallography 51, (2018).

61. Burger, V. M., Arenas, D. J. & Stultz, C. M. A Structure-free Method for Quantifying Conformational Flexibility in proteins. Scientific Reports 6, (2016)

62. Shen, B. W. et al. The tertiary structure and domain organization of coagulation factor VIII. Blood 111, 1240–1247 (2008).

63. Gilbert, G. E., Novakovic, V. A., Kaufman, R. J., Miao, H. & Pipe, S. W. Conservative mutations in the C2 domains of factor VIII and factor V alter phospholipid binding and cofactor activity. Blood 120, 1923–1932 (2012).

64. Novakovic, Valerie A., et al. "Membrane-Binding Properties of the Factor VIII C2 Domain." *Biochemical Journal*, vol. 435, no. 1, 187–196 (2011).

65. Schroeder, H. W. J. & Cavacini, L. Structure and Function of Immunoglobulins (author manuscript). J. Allergy Clin. Immunol. 125, S41–S52 (2010).

66. Meeks, S. L., Healey, J. F., Parker, E. T., Barrow, R. T. & Lollar, P. Nonclassical anti-C2 domain antibodies are present in patients with factor VIII inhibitors. Blood 112, 1151– 1153 (2008).

67. Jacques, David A., and Jill Trewhella. "Small-Angle Scattering for Structural Biology-Expanding the Frontier While Avoiding the Pitfalls." *Protein Science*, vol. 19, no. 4, 642–657 (2010).

68.Pratt, Kathleen P., et al. "Structure of the C2 Domain of Human Factor VIII at 1.5 Å Resolution." *Nature*, vol. 402, no. 6760, 439–442. (1999).

69. Spiegel, Paul Clint, et al. "Structure of a Factor VIII C2 Domain–Immunoglobulin G4K Fab Complex: Identification of an Inhibitory Antibody Epitope on the Surface of Factor VIII." *Blood*, vol. 98, no. 1, 13–19 (2001).

70. Brison, Caileen M., et al. "The 1.7 Å X-Ray Crystal Structure of the Porcine Factor VIII C2 Domain and Binding Analysis to Anti-Human C2 Domain Antibodies and Phospholipid Surfaces." *PLOS ONE*, vol. 10, no. 3, (2015).

71. Walter, J. D. et al. Thrombosis and hemostasis: Structure of the factor VIII C2 domain in a ternary complex with 2 inhibitor antibodies reveals classical and nonclassical epitopes. Blood 122, 4270–4278 (2013).

72. Giles, A. R., Mann, K. G. & Nesheim, M. E. A combination of factor Xa and phosphatidylcholine-phosphatidylserine vesicles bypasses factor VIII in vivo. Br. J. Haematol. 69, 491–497 (1988)., shaun 51) (Gilbert, G. E., Furie, B. C. & Furie, B. Binding of human factor VIII to phospholipid vesicles. J. Biol. Chem. 265, 815–822 (1990).

73. Gilbert, G. E. & Drinkwater, D. Specific Membrane Binding of Factor VIII Is Mediated by O-Phospho-L-serine, a Moiety of Phosphatidylserine. Biochemistry 32, 9577–9585 (1993).

74. Jesper J. Madsen, Y. Zenmei Ohkubo, Günther H. Peters, Johan H. Faber, E. & Tajkhorshid, and O. H. O. Membrane interaction of the factor VIIIa discoidin domains in atomistic detail. Biochemistry 54, 6123–6131 (2015).

75. Liu, M. L. et al. Hemophilic factor VIII C1- and C2-domain missense mutations and their modeling to the 1.5-angstrom human C2-domain crystal structure. Blood 96, 979–987 (2000).

76. Nguyen, Phuong-Cac T., et al. “High-Resolution Mapping of Epitopes on the C2 Domain of Factor VIII by Analysis of Point Mutants Using Surface Plasmon Resonance.” Blood, vol. 123, no. 17, 2732–2739, (2014).

77. Gao, Xiang, et al. “Prediction of Disulfide Bond Engineering Sites Using a Machine Learning Method.” *Scientific Reports*, vol. 10, no. 1, (2020).

78. Tsai, Pei Lun, et al. “Mass Spectrometry-Based Strategies for Protein Disulfide Bond Identification.” *Reviews in Analytical Chemistry*, vol. 32, no. 4, (2013).

79. Hsu, T. C., Pratt, K. P. & Thompson, A. R. The factor VIII C1 domain contributes to platelet binding. Blood 111, 200–208 (2008).

80. Lobstein, J. et al. SHuffle, a novel *E. coli* protein expression strain capable of correctly folding disulfide bonded proteins in its cytoplasm. Microb. Cell Fact. 11, 1 (2012).

81. Takeyama, Masahiro, et al. “Contribution of Factor VIII A2 Domain Residues 400–409 to a Factor X-Interactive Site in the Factor Xase Complex.” *Thrombosis and Haemostasis*, vol. 118, no. 05, 830–841, (2018).

82. Ivaskevicius, V., et al. “Coagulation Factor XIII Deficiency.” *Hämostaseologie*, vol. 34, no. 02, pp. 160–166., (2014).

83. Peters, Shaun C., "Structural and Mutational Characterization of the Blood Coagulation Factor VIII C Domain Lipid Binding Interface" (2021). *WWU Graduate School Collection*. 1068. https://cedar.wwu.edu/wwuet/1068

Appendix

C1C2_H2031C_V2294C_pET-32a(+)

MSDKIIHLTDDSFDTDVLKADGAILVDFWAEWCGPCKMIAPILDEIADEYQGKLTVAKLNIDQNPGTAPKYGIRGIPTLLL
FKNGEVAATKVGALSKGQLKEFLDANLAGSGSGHMHHHHHHSSGLVPRGSGMKETAAAKFERQHMDSPDLGTDDD
DKAMADIGSENLYFQSNSNKCQTPLGMASGCIRDFQITASGQYGQWAPKLARLHYSGSINAWSTKEPFSWIKVDLLAP
MIIHGIKTQGARQKFSSLYISQFIIMYSLDGKKWQTYRGNSTGTLMVFFGNVDSSGIKHNIFNPPIIARYIRLHPTHYSIRST
LRMELMGCDLNSCSMPLGMESKAISDAQITASSYFTNMFATWSPSKARLHLQGRSNAWRPQVNNPKEWLQVDFQK
TMKVTGVTTQGVKSLLTSMYVKEFLISSSQDGHQWTLFFQNGKVKVFQGNQDSFTPVCNSLDPPLLTRYLRIHPQSWV
HQIALRMEVLGCEAQDLY

C1C2_T2023C_V2294C__pET-32a(+)

MSDKIIHLTDDSFDTDVLKADGAILVDFWAEWCGPCKMIAPILDEIADEYQGKLTVAKLNIDQNPGTAPKYGIRGIPTLLL
FKNGEVAATKVGALSKGQLKEFLDANLAGSGSGHMHHHHHHSSGLVPRGSGMKETAAAKFERQHMDSPDLGTDDD
DKAMADIGSENLYFQSNSNKCQCPLGMASGHIRDFQITASGQYGQWAPKLARLHYSGSINAWSTKEPFSWIKVDLLAP
MIIHGIKTQGARQKFSSLYISQFIIMYSLDGKKWQTYRGNSTGTLMVFFGNVDSSGIKHNIFNPPIIARYIRLHPTHYSIRST
LRMELMGCDLNSCSMPLGMESKAISDAQITASSYFTNMFATWSPSKARLHLQGRSNAWRPQVNNPKEWLQVDFQK
TMKVTGVTTQGVKSLLTSMYVKEFLISSSQDGHQWTLFFQNGKVKVFQGNQDSFTPVCNSLDPPLLTRYLRIHPQSWV
HQIALRMEVLGCEAQDLY

C1C2_T2023_S2175_pET-32a(+)

MSDKIIHLTDDSFDTDVLKADGAILVDFWAEWCGPCKMIAPILDEIADEYQGKLTVAKLNIDQNPGTAPKYGIRGIPTLLL
FKNGEVAATKVGALSKGQLKEFLDANLAGSGSGHMHHHHHHSSGLVPRGSGMKETAAAKFERQHMDSPDLGTDDD
DKAMADIGSENLYFQSNSNKCQCPLGMASGHIRDFQITASGQYGQWAPKLARLHYSGSINAWSTKEPFSWIKVDLLAP
MIIHGIKTQGARQKFSSLYISQFIIMYSLDGKKWQTYRGNSTGTLMVFFGNVDSSGIKHNIFNPPIIARYIRLHPTHYSIRST
LRMELMGCDLNSCCMPLGMESKAISDAQITASSYFTNMFATWSPSKARLHLQGRSNAWRPQVNNPKEWLQVDFQK
TMKVTGVTTQGVKSLLTSMYVKEFLISSSQDGHQWTLFFQNGKVKVFQGNQDSFTPVVNSLDPPLLTRYLRIHPQSWV
HQIALRMEVLGCEAQDLY

C1C2_T2023C_L2324C_pET-32a(+)

MSDKIIHLTDDSFDTDVLKADGAILVDFWAEWCGPCKMIAPILDEIADEYQGKLTVAKLNIDQNPGTAPKYGIRGIPTLLL
FKNGEVAATKVGALSKGQLKEFLDANLAGSGSGHMHHHHHHSSGLVPRGSGMKETAAAKFERQHMDSPDLGTDDD
DKAMADIGSENLYFQSNSNKCQCPLGMASGHIRDFQITASGQYGQWAPKLARLHYSGSINAWSTKEPFSWIKVDLLAP
MIIHGIKTQGARQKFSSLYISQFIIMYSLDGKKWQTYRGNSTGTLMVFFGNVDSSGIKHNIFNPPIIARYIRLHPTHYSIRST
LRMELMGCDLNSCSMPLGMESKAISDAQITASSYFTNMFATWSPSKARLHLQGRSNAWRPQVNNPKEWLQVDFQK
TMKVTGVTTQGVKSLLTSMYVKEFLISSSQDGHQWTLFFQNGKVKVFQGNQDSFTPVVNSLDPPLLTRYLRIHPQSWV
HQIALRMEVCGCEAQDLY

Appendix Figure 1. Complete FVIII C1C2 Disulfide Mutant Construct Sequences. Sequences were ordered from Genescript. FVIII C1C2 domain sequence is highlighted in green, thioredoxin in yellow, 6x-His tag in cyan, TEV cleavage site in grey, and mutations in red.

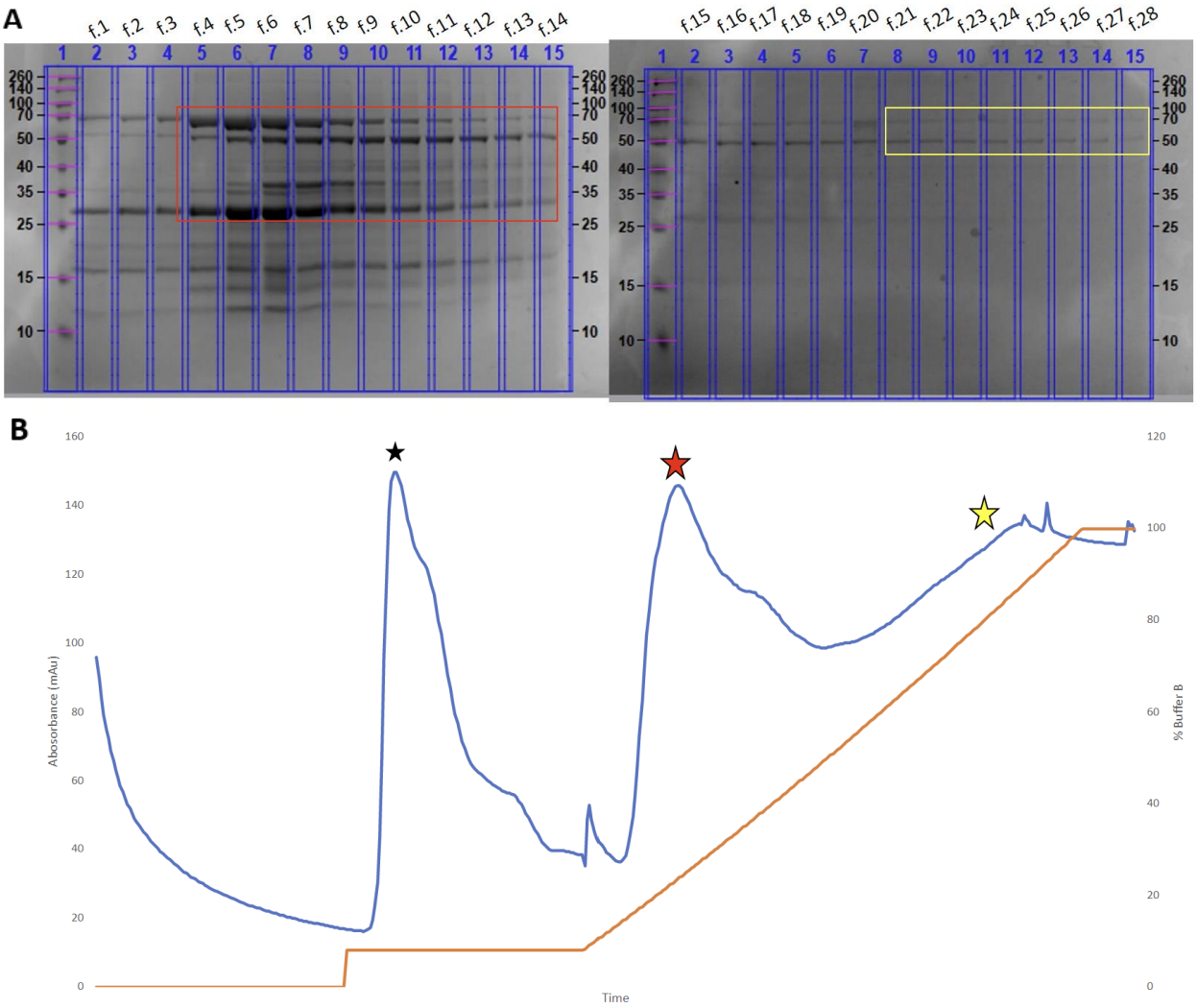

Appendix Figure 2. C1C2 disulfide mutant purification. A) SDS-PAGE gel image of C1C2 T2023C/L2324C FPLC NI-NTA purification, with fraction number X labeled as f. X. Non-pure samples are boxed in red and pure samples are boxed in yellow, corresponding to the red and yellow stars on the chromatograph. B) Ni-NTA chromatogram of C1C2 T2023C, L2324C purification, absorbance shown by the blue curve, and % buffer B shown by the orange curve. The black star shows the end of the ATP wash and the elution of the 70 kDa contaminant, the red star shows the beginning of elution off the column, matching the fractions boxed in red on the gel image, and the yellow star shows the elution of the purified sample, corresponding to the yellow boxed fractions on the gel image.

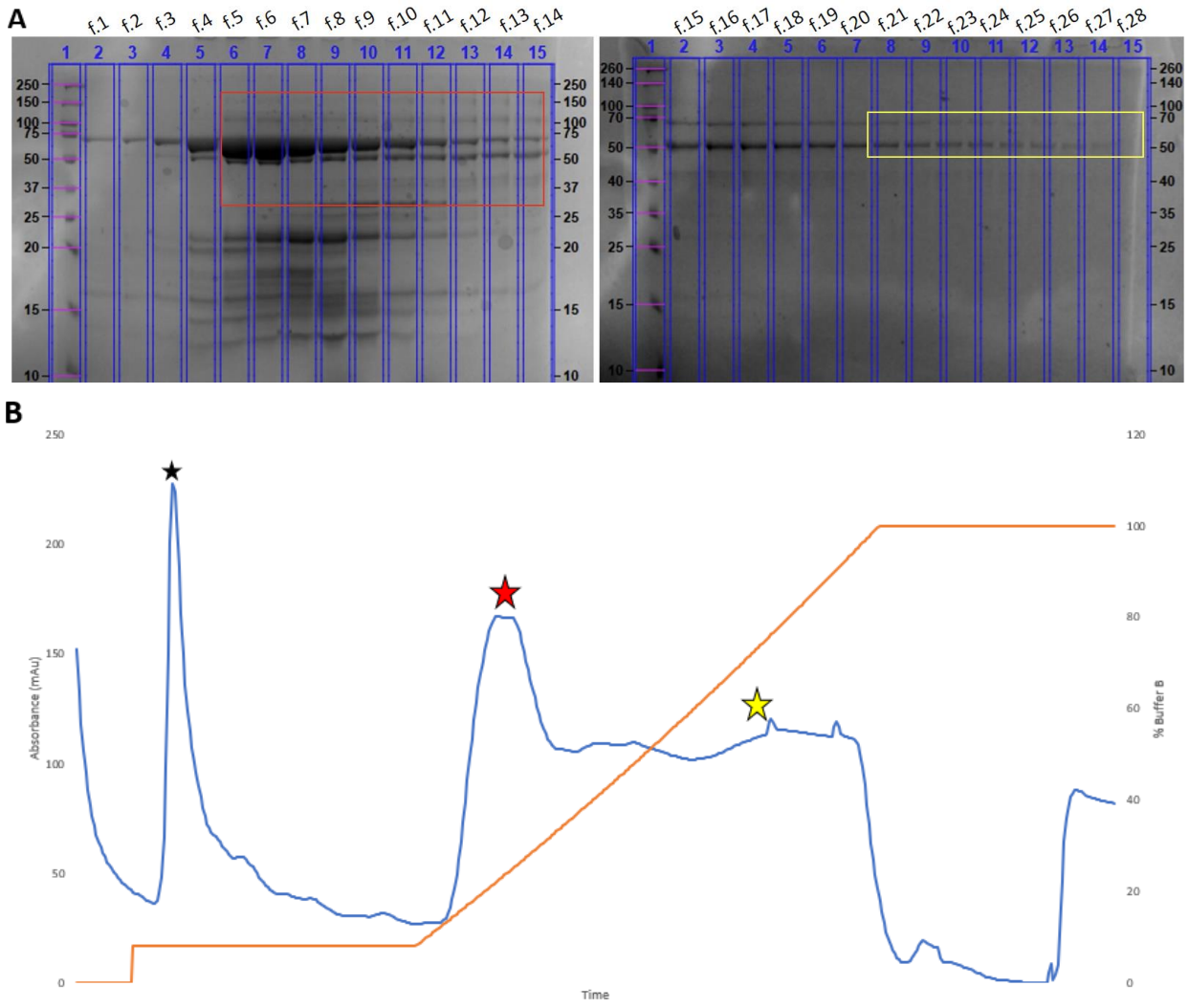

Appendix Figure 3. C1C2 disulfide mutant purification. A) SDS-PAGE gel image of C1C2 T2023C/V2294C FPLC NI-NTA purification, with fraction number X labeled as f. X. Non-pure samples are boxed in red and pure samples are boxed in yellow, corresponding to the red and yellow stars on the chromatograph. B) Ni-NTA chromatogram of C1C2 T2023C, V2294C purification, absorbance shown by the blue curve, and % buffer B shown by the orange curve. The black star shows the end of the ATP wash and the elution of the 70 kDa contaminant, the red star shows the beginning of elution off the column, matching the fractions boxed in red on the gel image, and the yellow star shows the elution of the purified sample, corresponding to the yellow boxed fractions on the gel image.

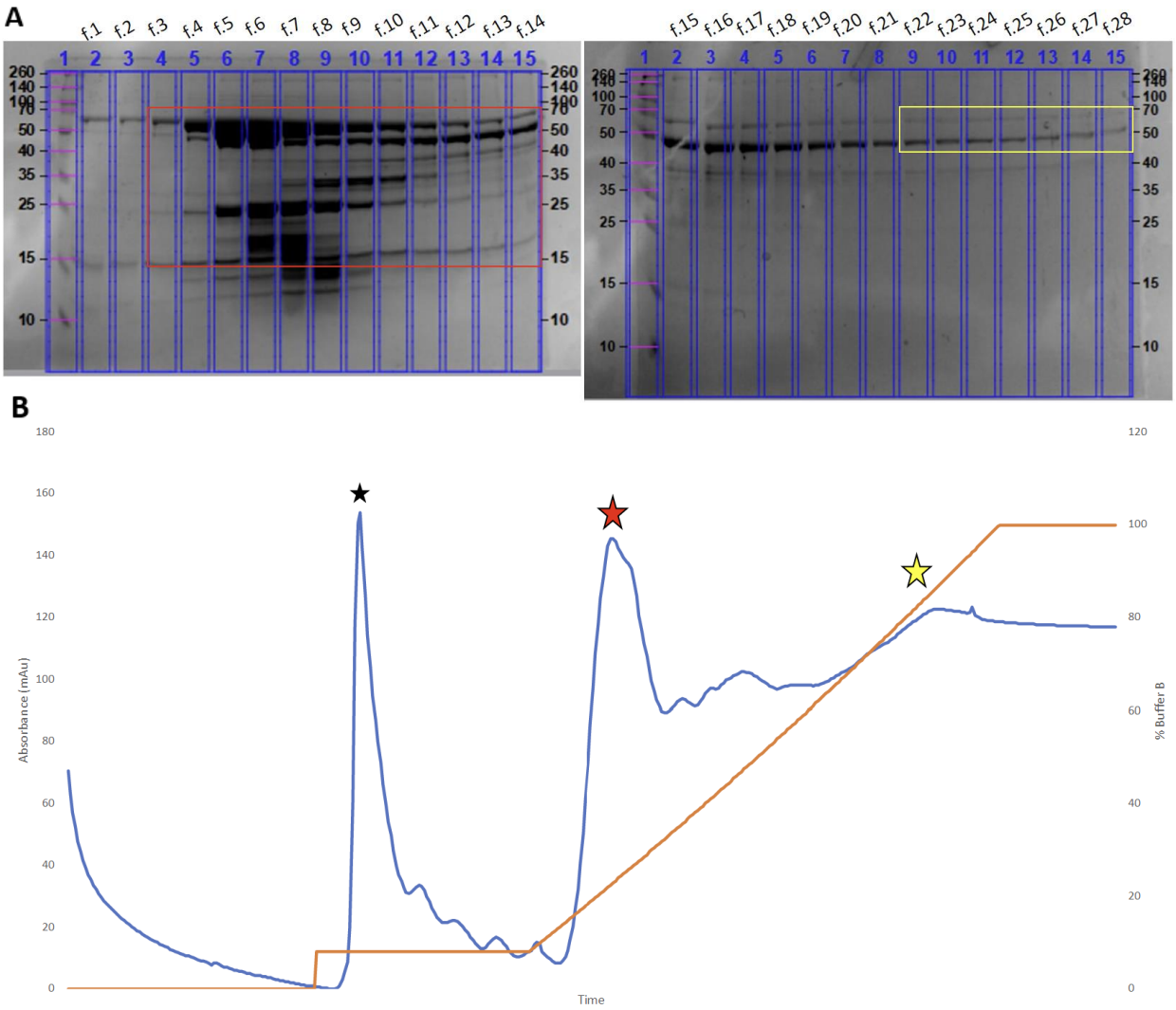

Appendix Figure 4. C1C2 disulfide mutant purification. A) SDS-PAGE gel image of C1C2 H2031C/V2294C FPLC NI-NTA purification, with fraction number X labeled as f. X. Non-pure samples are boxed in red and pure samples are boxed in yellow, corresponding to the red and yellow stars on the chromatograph. B) Ni-NTA chromatogram of C1C2 H2031C, V2294C purification, absorbance shown by the blue curve, and % buffer B shown by the orange curve. The black star shows the end of the ATP wash and the elution of the 70 kDa contaminant, the red star shows the beginning of elution off the column, matching the fractions boxed in red on the gel image, and the yellow star shows the elution of the purified sample, corresponding to the yellow boxed fractions on the gel image.

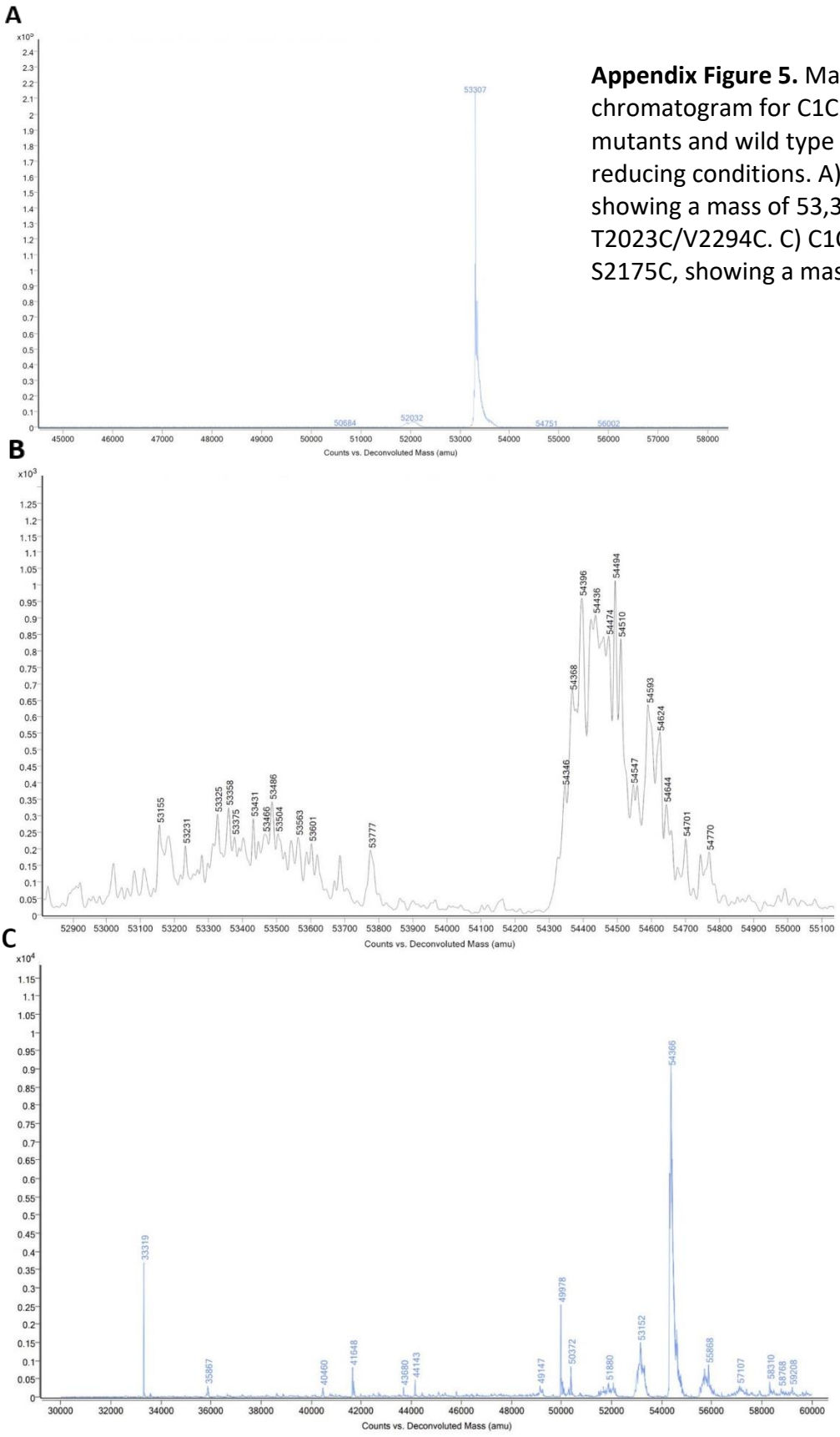

Appendix Figure 5. Mass chromatogram for C1C2 disulfide mutants and wild type under non-reducing conditions. A) C1C2 WT, showing a mass of 53,307 Da. B) C1C2 T2023C/V2294C. C) C1C2 T2023C, S2175C, showing a mass of 54,366 Da.